

RICE UNIVERSITY

**Sheet Fluorescence and Annular Analysis of
Ultracold Neutral Plasmas**

by

Jose Antonio Castro Nieto

A THESIS SUBMITTED
IN PARTIAL FULFILLMENT OF THE
REQUIREMENTS FOR THE DEGREE

Master of Science

APPROVED, THESIS COMMITTEE:

Thomas C. Killian, Chair
Associate Professor of Physics and
Astronomy

Randall G. Hulet
Fayez Sarofim Professor of Physics and
Astronomy

Anthony A. Chan
Professor of Physics and Astronomy

Houston, Texas

October, 2009

Abstract

Sheet Fluorescence and Annular Analysis of Ultracold Neutral Plasmas

by

Jose Antonio Castro Nieto

This thesis describes sheet fluorescence and annular analysis in strontium ultracold neutral plasmas (UNPs). UNPs are interesting because they can be strongly-coupled, where strong-coupling indicates plasmas with Coulomb interaction energies higher than their thermal energy. UNPs are ideal for studying strongly-coupled physics since they offer the ability to precisely control their initial conditions. Previous studies of UNPs applied fluorescence spectroscopy to measure expansion and ion temperature. This thesis further refines fluorescence by narrowing the laser into a sheet, thereby measuring parameters in the plasma where density variation is small. Annular analysis increases the signal-to-noise ratio in these measurements by adding the signal from sections of an annulus in the spherically-symmetric plasma. This method is applied to the study of kinetic energy oscillations in UNPs, obtaining a higher resolution than previous experiments, and may be used for other density dependent studies.

Acknowledgments

Firstly, I would like to thank my advisor Tom Killian for his guidance. I especially want to thank you for showing me how to properly conduct and communicate science. I would also like to thank my committee members, Prof. Randy Hulet and Prof. Anthony Chan for agreeing to review my work. I want to acknowledge the support given by the Department of Energy Office of Fusion Energy Sciences, the National Science Foundation, the David and Lucille Packard Foundation, the Ministerio de Ciencia y Tecnología, Costa Rica (MICIT) and the Consejo Nacional para Investigaciones Científicas y Tecnológicas, Costa Rica (CONICIT).

I could not accomplish any of this work without the help of my labmates, especially the former senior graduate students in the experiment Priya Gupta, Sampad Laha and Clayton Simien, and our former post doc Hong Gao, who helped me improve my experimental skills. Patrick, even though you are new to our experiment, you have been an enormous help and relief for me. Sarah, Pascal, Natali, Dan, Mi and Brian, even though you are not directly involved with my research, discussions with you guys about physics and your experiments have always been fruitful.

I also want to thank my father Felipe and my mother Nelly for providing me with the love, tools and environment to flourish. My brother Felipe and my sister Marianela have always been there for me and I thank you for that. Finally I want to thank my wife, Maricruz for making all my days shine! You are my favorite person.

Contents

Abstract	ii
Acknowledgments	iii
1 Introduction	1
2 Ultracold Neutral Plasmas	6
2.1 Creation of ultracold neutral plasmas	6
2.2 Dynamics of ultracold neutral plasmas	10
2.2.1 Disorder-induced heating	10
2.2.2 Kinetic energy oscillations	13
2.2.3 Self similar adiabatic expansion	14
2.2.4 Other physical processes	20
3 Annular analysis of sheet fluorescence spectroscopy	21
3.1 Sheet fluorescence	21
3.2 Description of annular analysis	30
4 Application of annular analysis to kinetic energy oscillation measurements	42
5 Conclusions	46
Bibliography	48
Appendices	53
A Improvements in ionization fraction	53

B MATLAB code for annular analysis	58
C Calibration of imaging resolution	59

Chapter 1

Introduction

Ultracold neutral plasmas (UNP) are quasineutral plasmas with very low thermal energies compared to traditional plasmas.¹ The electron temperature in UNPs ranges from 1 – 1000 K, ion temperatures around ~ 1 K, and densities as high as 10^{10} cm⁻³. Typical sizes for these plasmas are around 5 mm diameter with Debye lengths ranging from 1 – 10 μ m.

There are several methods for creating an ultracold neutral plasma. The first UNP was created by photoionization of laser-cooled and trapped xenon atoms in a magneto-optical trap (MOT),^{2,3} where the photoionizing laser was tuned just above the ionization continuum. This method of direct photoionization has since been applied to other laser-cooled atomic species such as strontium⁴ and calcium.⁵ Another method for creating a UNP involves tuning the ionizing laser wavelength just below the ionization threshold, producing a dense gas of highly excited Rydberg atoms in which electron-atom collisions can drive a spontaneous ionization cascade.^{6,7} Finally, ultracold plasmas can also be created from a recently developed method in which molecules seeded in a supersonic molecular beam can be excited to directly make a plasma or excited just below threshold to create a Rydberg gas that spontaneously ionizes to form a plasma.⁸

As mentioned above, upon creation, ultracold neutral plasmas possess low ther-

mal energy and are thus important in that they display physics of strongly-coupled systems.⁹ A strongly-coupled system is one in which the Coulomb interaction energy between nearest neighbors is comparable to or higher than their thermal energy. This can be mathematically described by the Coulomb coupling parameter,

$$\Gamma = \frac{e^2}{4\pi\epsilon_0 akT} > 1. \quad (1.1)$$

Here, T is the temperature and a is the Wigner-Seitz radius (mean inter-particle distance), $a = [3/(4\pi n)]^{1/3}$ for density n . As different species in the plasma can have different densities and/or temperatures, this results in different coupling parameters for different species. By virtue of their cold temperatures, UNPs can have strongly-coupled ions and electrons. Experiments in UNPs have shown that ions equilibrate with $2 < \Gamma_i < 5^{4,10}$ and electrons, while they can initially be strongly correlated, equilibrate with $\Gamma_e \leq 0.2$.^{11,12,13,14}

Equation 1.1 implies that strong-coupling requires high densities and/or low temperatures, conditions which make the experimental study of strong-coupling quite challenging. Some examples of environments with these extreme conditions can be found in astrophysics,¹⁵ dusty plasmas,¹⁶ non-neutral trapped ion plasmas¹⁷ and plasmas with potential industrial applications such as intense-laser/matter interactions^{18,19} and in inertial confinement fusion experiments.^{20,21,22,23}

In contrast, ultracold neutral plasmas have several advantages that make them an excellent “model system” to study strong-coupling. Firstly, their formation mechanism makes the initial conditions of UNPs precisely controllable, allowing for versatility in

the experiments. Next, with the exception of ion and dusty plasmas, UNPs have longer time scales due to their lower densities, and this allows the measurement of important physical quantities. Additionally, UNPs are quasineutral, which enables the study of phenomena involving two species such as equilibration and recombination. Finally, measurements in UNPs can be performed with non-invasive optical diagnostics that do not perturb the medium. As a result of these advantages, ultracold neutral plasmas provide an experimental realization of strong-coupling and a platform to probe and study the physics of this regime.^{24,1}

It is important to study strong-coupling because traditional plasma physics concepts such as hydrodynamics become invalid in strongly-coupled plasmas. Additionally, strong-coupling implies the development of spatial correlations between particles, and new phenomena like disorder-induced heating and kinetic energy oscillations have been observed.^{25,26,27}

Expansion of ultracold neutral plasmas can also relate to the physics of plasmas produced with short-pulse laser irradiation of solid, liquid, foil, and cluster targets.^{20,21,22,23} The expansion of UNPs into the surrounding vacuum has been studied^{28,29,27,30,11,31,4,32,5,33,34} as well as the electron dynamics during the expansion.^{12,13,11,35,14}

The experimental work mentioned above was performed on samples with non-uniform density profiles. As such these previous results have to be interpreted as averaged over the density distribution of the plasma. However, important physical quantities in strongly-coupled systems, such as relaxation times and temperature,

have a strong dependence on density. To understand the dependence upon density of these physical quantities, it is crucial to develop an experimental technique in which one can study strongly-coupled systems with small density variations. Further understanding of the thermal properties and equilibration of such strongly-coupled systems would advance basic understanding and potential applications of these plasmas.

It is challenging to measure and characterize regions in UNPs where density variations are small. Ultracold neutral plasmas usually have a Gaussian density distribution^{4,34} and regions with small density variation are usually small and thus measurements of them possess a very small signal-to-noise ratio. This thesis will focus on the use of annular analysis to allow higher signal-to-noise ratio in sheet fluorescence measurements by summing contributions from regions of the ultracold neutral plasma with similar density.

Chapter 2 of this thesis will provide a description of the creation of UNPs by direct photoionization of laser-cooled strontium atoms. Chapter 2 will also present the physics of important dynamical processes of UNPs in general. Chapter 3 provides a description of the sheet fluorescence diagnostic that measures the physical quantities in ultracold neutral plasmas, along with the theory behind this experimental technique. This chapter will also showcase annular analysis of sheet fluorescence spectroscopy as a method for obtaining higher signal-to-noise ratio and resolution from fluorescence signals. An implementation of this method of analysis will be presented in chapter 4 in its application to a dynamical process in UNPs, namely kinetic energy

oscillations. Conclusions to this thesis will be presented in chapter 5. Finally the appendices will present complementary information, which include improvements of the ionization fraction in the plasma (Appendix A), the MATLAB code for annular analysis of images (Appendix B) and finally a calibration of our imaging resolution (Appendix C).

Chapter 2

Ultracold Neutral Plasmas

2.1 Creation of ultracold neutral plasmas

We create our ultracold neutral plasma through direct ionization of laser-cooled trapped strontium atoms^{36,4} in a magneto-optical trap (MOT). Details on laser cooling can be found in Metcalf and van der Straten.² Our experimental setup is shown in Fig. 2.1. It is a three beam retro-reflected MOT operating on the dipole-allowed $^1S_0 - ^1P_1$ transition at 461 nm. This transition has a linewidth, $\gamma = 32$ MHz, and a saturation intensity, $I_{sat} = 42.5$ mW/cm². The MOT beams have an intensity of $I = 19$ mW/cm² $\leq I_{sat}$ with a 7.5 mm waist, red detuned by 79 MHz from resonance. Atoms are loaded from an atomic beam cooled by a 2D collimator (not shown in the image) and a Zeeman slower. The 2D collimator, consisting of two retroreflected beams in a cross pattern perpendicular to the atomic beam, reduces the atoms' transverse velocity. The beams have 60 mW of power and are red detuned by 20 MHz. To slow the atoms longitudinally, the Zeeman beam propagates opposite to the direction of the atomic beam. It has 150 mW of power and is red detuned by 530 MHz from resonance. The combination of these beams, along with two magnetic coils in anti-Helmholtz configuration, creates a trap for cooling the strontium atoms.

The laser-cooled atom cloud is characterized by a temperature of ~ 10 mK, where

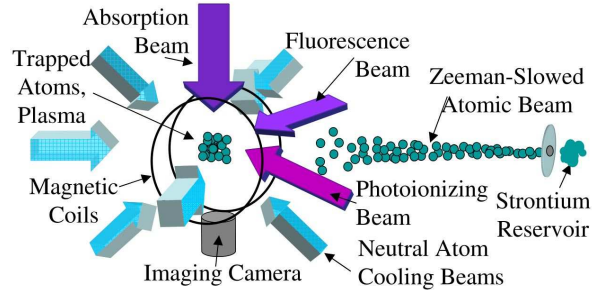


Figure 2.1 : Experimental set-up for ultracold neutral plasma experiments. Neutral strontium atoms from a reservoir are Zeeman-slowed and enter the trapping region. The magneto-optical trap (MOT) consists of a pair of anti-Helmholtz magnetic coils and six laser-cooling beams. 1P_1 trapped atoms are then ionized by the photoionizing laser. The fluorescence probe beam propagates in a direction that is perpendicular to the imaging axis and CCD camera. The complementary absorption probe beam passes through the plasma and falls on the camera.

as we shall later see, the exact temperature of the MOT is not critical to our experiment. The atomic cloud has a spherically symmetric Gaussian density distribution, $n(r) = n_0 \exp(-r^2/2\sigma^2)$, with $\sigma \approx 0.6$ mm and $n_0 \approx 6 \times 10^{10}$ cm $^{-3}$.³⁷ The number of trapped atoms is typically 2×10^8 . To obtain larger samples, with corresponding lower densities, we can turn off the trap to allow the cloud to expand.

Photoionization of the atoms is performed by two overlapping ~ 10 ns laser pulses: one from an amplified laser tuned to the cooling transition of the atoms ($^1S_0 - ^1P_1$) at 461 nm and the second one from a dye laser tuned just above the ionization continuum at ~ 412 nm (Fig. 2.2 A). Two laser pulses are used for photoionization instead of only one UV pulse, as the latter would be harder to implement experimentally. Additionally, certain dynamical process in the plasma, such as Rydberg-electron collisions, occur on time scales of $\sim 10 - 100$ ns,^{30,11,31,38} reinforcing the need for short photoionizing pulses.

The ionization fraction is limited by the number of excited state atoms (product of the first laser pulse) and the energy of the photoionizing beam (second laser). To increase the number of excited atoms, the first laser is pulse-amplified in a dye cell pumped by a pulsed Nd:YAG laser. Pulse-amplification of the excitation beam drastically increases the number of excited strontium atoms. Details of the implementation of this pulse-amplified beam can be found in Appendix A. To then photoionize a good fraction of the excited atoms, we use a high-energy tunable dye laser pumped by the same pulsed Nd:YAG laser.³⁸ Appendix A also includes a brief description of improvements to the dye circulation system of the photoionizing dye laser to further increase our ionization fraction and to ensure repeatability.

Pulse-amplification and improvements to the dye laser brought about ionization fractions of 75%. As the density profiles of the plasma components, $n_e(r) \approx n_i(r)$, follow the Gaussian shape of the neutral atom cloud, this results in peak electron and ion densities as high as $n_{0e} \approx n_{0i} \approx 4.5 \times 10^{10} \text{ cm}^{-3}$.

After photoionization a plasma is created and most of the remaining energy from the photoionizing beam (difference between the photon energy and the ionization potential) is acquired by the electrons. If the ions and electrons are initially considered at rest, energy conservation for the pulsed laser photons of frequency ν gives an excess energy $\Delta E = h\nu - E_{IP} = p_i^2/(2m_i) + p_e^2/(2m_e)$, where the ionization potential is E_{IP} . Momentum conservation, on the other hand, will give $\hbar\mathbf{k} = \mathbf{p}_i + \mathbf{p}_e$. If we assume the photon momentum $k = |\mathbf{k}|$ is small (for $T_e = 10 \text{ K}$, $(\hbar k)^2 \approx \langle p_e^2 \rangle / 100$), then

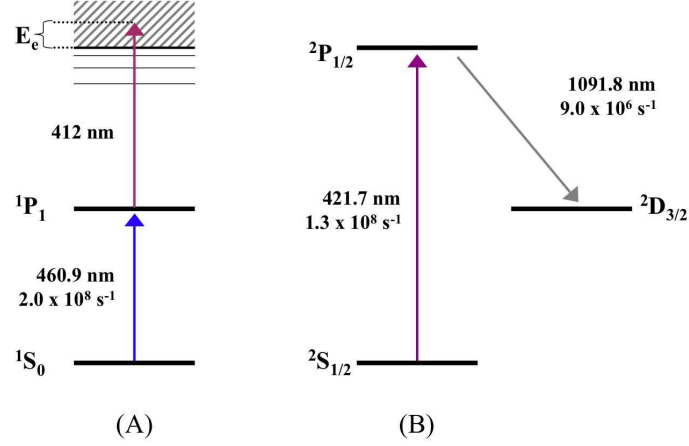


Figure 2.2 : Atomic and ionic energy levels involved in strontium experiments, with decay rates. (A) Neutral atoms are laser-cooled and trapped in a magneto-optical trap (MOT) operating on the $^1S_0 - ^1P_1$ transition at 460.9 nm, as described by Nagel *et al.*³⁶ Atoms are later excited to the 1P_1 level by a pulse-amplified laser and ionized by photons from a laser at ~ 412 nm. (B) Imaging of the ions is done on the $^2S_{1/2} - ^2P_{1/2}$ transition at 421.7 nm. $^2P_{1/2}$ ions decay to the $^2D_{3/2}$ state 7% of the time, after which they cease to interact with the imaging beam. The intensity and duration of the 422 nm light is low enough to avoid optical pumping to this metastable $^2D_{3/2}$ state.

$\mathbf{p}_i \approx -\mathbf{p}_e$. Due to the small electron-ion mass ratio, the ion kinetic energy is thus much smaller than the electron kinetic energy, and the electrons take away essentially all the excess photon energy, ΔE , as kinetic energy: $E_e = p_e^2 / (2m_e) \approx \Delta E$. Our photoionizing beam comes from a tunable dye laser and if we vary ν , we can produce electrons with initial kinetic energies typically between 1 and 1000 K. The ion kinetic energy will be $p_i^2 / (2m_i) \approx p_e^2 / (2m_i) = \Delta E (m_e / m_i)$, which is only on the order of millikelvin even for $\Delta E / k_B = 1000$ K. Therefore, the initial kinetic energy for the ions is close to the kinetic energy of neutral atoms in the MOT.

This direct photoionization method of creating ultracold neutral plasmas enables precise control of the initial conditions of the plasma. The density profile and size of

the plasma closely follow those of the trapped cold atoms. These are experimentally controlled by varying the intensity and power balance of the trapping lasers. The same is also true for the initial kinetic energy of the ions. On the other hand, the initial kinetic energy of the electrons is easily tuned by changing the frequency of the pulsed dye laser. Finally, the peak density of the plasma can be controlled through the peak density of the trapped atoms in combination with the intensity of the photoionizing beam. As we shall see, this is important as the initial conditions of the plasma ($T_{i,e}$ and $n_{i,e}$) will strongly affect the dynamics and evolution of the ultracold plasma.

2.2 Dynamics of ultracold neutral plasmas

2.2.1 Disorder-induced heating

Upon creation of the plasma, both electrons and ions are in a spatially uncorrelated state. Even though both species inherit the spherically symmetric Gaussian distribution of the atoms, they are located randomly with respect to their neighbors and as a result, possess a lot of potential energy. To establish equipartition between potential and kinetic energy, the plasma goes through a process called disorder-induced heating (DIH).

To lower their potential energy, electrons and ions move to a more ordered and correlated state. This process happens in an adiabatic environment, and so the total energy has to be conserved. As correlations develop, the particles' potential energy is converted into (thermal) kinetic energy and the plasma heats up.

These correlations develop on different time scales for each species, given by the inverse plasma frequency, $\omega_{p\alpha}^{-1} = \sqrt{m_\alpha \epsilon_0 / (n_\alpha e^2)}$, where m_α and n_α are, respectively the mass and density and α denotes the plasma species (i for ions and e for electrons). For the electron densities in our experiment, ω_{pe}^{-1} corresponds to a few nanoseconds. It has been shown that while the electrons can be created with low kinetic energy, this rapid increase in the electron kinetic energy due to DIH produces, in combination with other processes such as three body recombination, an electron coupling parameter $\Gamma_e \leq 0.2$.^{11,12,39,13,14}

In the case of ions, both ω_{pi}^{-1} and the timescales for DIH are on the order of 1 μ s. Murillo calculated the disorder-induced heating temperature for the ions.²⁷ These calculations assume electron screening of the Coulomb interactions between ions, resulting in a Yukawa potential for the ions, $U(r) = \exp(-r/\lambda_{D,e})[e^2/(4\pi\epsilon_0 r)]$. The equilibrium temperature is then given by

$$T_i = \frac{2}{3} \frac{e^2}{4\pi\epsilon_0 a(n_i)k_B} \left| \tilde{U}[\kappa, \Gamma_i(n_i, T_i)] + \frac{\kappa(n_i, T_e)}{2} \right|. \quad (2.1)$$

Here, $\kappa = a/\lambda_{D,e}$ and $\lambda_{D,e} = \sqrt{\epsilon_0 k_B T_e / (n_e e^2)}$ is the electron Debye screening length. As mentioned before, a typical value of the electron Debye length is from 1 to 10 μ m. \tilde{U} in the above equation is the equilibrium potential energy per particle, or “excess energy” per particle in units of $e^2/(4\pi\epsilon_0 a)$ and it depends on the equilibrium Γ_i . Values for \tilde{U} were tabulated by Hamaguchi, Farouki and Dubin⁴⁰ using a molecular dynamics simulation.

As T_i varies with $\Gamma_i(n_i, T_i)$, Eq. 2.1 has to be solved numerically using iterative

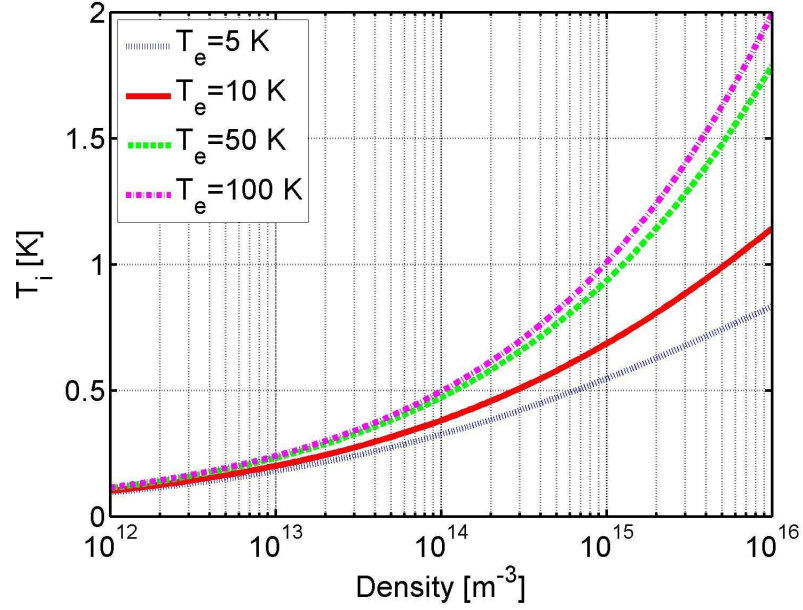


Figure 2.3 : Equilibrium ion temperature, T_i , after disorder-induced heating for varying density, n_i , and electron temperature, T_e . Increasing n_i and/or T_e , increases the ion-ion Coulomb interaction and resulting T_i . The equilibrium ion temperature is calculated from the numerical solution of Eq. 2.1.

techniques.⁴¹ The results from equation 2.1 were confirmed experimentally by Simien, Chen and Laha.^{4,25,26} Figure 2.3 shows a plot of the calculated DIH temperature as it changes with density and electron temperature. Increasing density (decreasing inter-particle spacing), results in more Coulomb interactions, which results in a higher DIH temperature. Increasing electron temperature decreases their screening; this increases the Coulomb forces between the ions producing a higher DIH temperature.²⁵

To summarize, as a result of this DIH phase, within hundreds of nanoseconds, electrons heat up by a few kelvin and attain a corresponding temperature of $T_e \approx 2E_e/(3k_B)$. On the other hand, the initially much colder ions (T_i on the order of a few mK), gain relatively more energy from disorder-induced heating and will attain

energies of $E_i/k_B \sim 1K$.

2.2.2 Kinetic energy oscillations

As mentioned above, DIH occurs on the time scales of the inverse plasma frequency, $\omega_{pi}^{-1} = \sqrt{m_i \epsilon_0 / (n_i e^2)}$. Quite simply, this is the time that an ion takes to travel through a distance of $a = [3/(4\pi n_i)]^{1/3}$ under a restoring Coulomb force of $e^2/(4\pi \epsilon_0 a^2)$. It was clearly seen by Chen and Laha^{25,26} that during disorder-induced heating, the temperature reaches a local maximum, followed by a local minimum with an ensuing oscillation.

The ion temperature oscillates because the ions overshoot the lowest potential energy state, oscillating in a potential well with an exchange between the potential and kinetic energy until they settle at the bottom of the well. This oscillatory picture is only appropriate in a system where the correlation energy between particles is greater than the thermal energy, namely strongly-coupled plasmas such as UNPs.

The oscillations happen at a frequency of $2\omega_{pi}$. Since the ion plasma frequency varies with density, ions at different locations in the plasma oscillate at different frequencies. In the Gaussian density profile of an ultracold neutral plasma, the inner region has higher density, resulting in a higher plasma oscillation frequency; the less dense outer region has a correspondingly lower plasma oscillation frequency.

These previous experiments used absorption imaging to perform kinetic energy oscillation measurements.^{25,26,41} However, the absorption imaging beam probes the

whole plasma cloud, averaging over the Gaussian density distribution. Because of this variation in ω_{pi} , this averaging over the entire cloud dephases the oscillations as explained by Chen and Laha.^{25,26,41} This leads to the observed reduced contrast in the oscillation, making it difficult to study the damping rate of such oscillations. As we shall see in the next chapter, sheet fluorescence imaging and annular analysis were developed to circumvent this averaging.

2.2.3 Self similar adiabatic expansion

Continuing with the physical processes in UNPs, after this initial ion heating and oscillation, the entire plasma expands into the surrounding vacuum. This expansion is a direct consequence of the thermal pressure produced by the electrons. Initially, electrons have high kinetic energy and tend to leave the plasma cloud. However, the Coulomb force due to the positive charge from the ions allows only a small percentage of the electrons to leave. The ions then experience a radial recoil force and the plasma expands. During the ensuing plasma expansion, the thermal energy of the electrons is converted into expansion energy of the ions. This expansion was studied theoretically in^{11,27,31,32,30} and was seen experimentally in.^{4,5,28,33,42,34,14} The expansion of an ultracold plasma is self-similar and the initial Gaussian profile is preserved as long as the initial $\Gamma_e < 1$.¹⁴ This last condition is violated at very high initial plasma density and very low initial electron temperature.¹⁴ The remainder of this section is a more thorough description of the expansion.

The expansion of ultracold plasmas can be described with a solution to the Vlasov kinetic equations. The Vlasov equations illustrate conservation of probability for an incompressible fluid. They can be used to describe the evolution of the ion and electron distribution functions in a plasma when collisions and radiative processes can be neglected.⁴³ An exact solution to this problem was identified for a 1-dimensional system by Baitin *et al.*⁴⁴ and extended to three dimensions by Dorozhkina *et al.*⁴³ Lastly, the exact solution to a self-similar Gaussian quasineutral plasma was described by Mora.⁴⁵

It must be noted that the Vlasov equations do not include any correlation effects and, as such, are strictly valid only for systems with $\Gamma \ll 1$. Electron correlations are not an issue during expansion since, as mentioned above, DIH and three-body recombination lower electron correlation to $\Gamma_e \leq 0.2$ within hundreds of nanoseconds.^{11,12,39,13,14} Ionic correlations were addressed by Pohl *et al.*³¹ by comparing the solutions to the Vlasov equation (kinetic approach) with a hybrid molecular dynamics simulation that included ionic correlations. It was shown in this work that the inclusion of ionic correlations does not change the qualitative behaviour of the expansion, and ultimately that the solutions to the Vlasov equations describe the experimental observables rather well. Laha *et al.*³⁴ showed in experiments how an expanding UNP is in fact a realization of an exact solution to the Vlasov equations in the absence of dissipative forces (electron-ion thermalization, collisions, or three-body recombination).

With these considerations in mind, let us then expand on this exact solution to the Vlasov equation. For the evolution of the one particle distribution function, $f_\alpha(\mathbf{r}, \mathbf{v})$, giving the probability of having a charged particle at position \mathbf{r} with velocity \mathbf{v} , the Vlasov equation can be written as

$$\frac{\partial f_\alpha}{\partial t} + \mathbf{v} \frac{\partial f_\alpha}{\partial \mathbf{r}} - \frac{q_\alpha}{m_\alpha} \frac{\partial \phi(\mathbf{r})}{\partial \mathbf{r}} \frac{\partial f_\alpha}{\partial \mathbf{v}} = 0. \quad (2.2)$$

Here, $\alpha = e, i$ for electrons and ions respectively, m_α and q_α are the mass and charge of the species α , and ϕ is the total mean-field potential.

To find a solution to Eq. 2.2, we have to make certain assumptions, all of which can be experimentally attained in UNPs. Firstly, we assume quasineutrality and obtain this experimentally since only a small fraction of the electrons escape, resulting in an electron and ion density that are almost the same locally. Secondly, we assume spherical Gaussian symmetry for the plasma which is obtained in the experiment through proper power balance of the trapping laser beams for the atomic cloud. As mentioned before, the plasma inherits the symmetry of the atomic cloud. Finally, we assume the adiabatic approximation for the electrons and imply that the electrons rethermalize rapidly with any change in the Coulomb potential in the system. This is justified as the time scales for electron equilibration are faster due to the small mass ratio m_e/m_i . We assume a Maxwellian distribution for the electrons,

$$f_e(\mathbf{r}, \mathbf{v}, t) \propto \exp\left\{\frac{e\phi(\mathbf{r})}{k_B T_e(t)}\right\} \exp\left\{-\frac{m_e v^2}{2k_B T_e(t)}\right\}, \quad (2.3)$$

where the electron temperature, T_e , has no dependence on r .³¹ This third and last

assumption is approximately realized as electrons in a UNP thermalize among themselves within a few nanoseconds.^{11,31}

Using the quasineutrality assumption ($n_e \approx n_i$) and substituting Eq. 2.3 into Eq. 2.2 (with $\alpha = e$), we can express the mean-field potential in terms of the ion density as¹

$$e \frac{\partial \phi}{\partial \mathbf{r}} = k_B T_e n_i^{-1} \frac{\partial n_i}{\partial \mathbf{r}}. \quad (2.4)$$

For a spherically symmetric Gaussian density distribution, this potential yields a linear force on an ion given by

$$\vec{F}(\vec{r}, t) = e \vec{E} = e \frac{\partial \phi}{\partial \mathbf{r}} = \frac{k_B T_e(t) \vec{r}}{\sigma(t)^2}. \quad (2.5)$$

Using this linear force, we can propose the following ansatz for the ion distribution function,

$$f_i(\mathbf{r}, \mathbf{v}) \propto \exp \left\{ -\frac{r^2}{2\sigma^2} \right\} \exp \left\{ -\frac{m_i [\mathbf{v} - \mathbf{u}(\mathbf{r}, t)]^2}{2k_B T_i} \right\}, \quad (2.6)$$

$$\mathbf{u}(\mathbf{r}, t) = \gamma(t) \mathbf{r}, \quad (2.7)$$

where $\gamma(t)$ parametrizes the hydrodynamic ion velocity. Next, we calculate the moments of Eq. 2.2 with the above ansatz to obtain the following sets of differential equations¹ which describe the evolution of the size, expansion velocity, and temperature of the plasma:

$$\frac{\partial \sigma^2}{\partial t} = 2\gamma \sigma^2, \quad (2.8)$$

$$\frac{\partial \gamma}{\partial t} = \frac{k_B T_e + k_B T_i}{m_i \sigma^2} - \gamma^2, \quad (2.9)$$

$$\frac{\partial(k_B T_i)}{\partial t} = -2\gamma k_B T_i, \quad (2.10)$$

$$\frac{\partial(k_B T_e)}{\partial t} = -2\gamma k_B T_e. \quad (2.11)$$

Equations 2.10 and 2.11 reflect the cooling of the ions and electrons as the plasma evolves. By multiplying Eq. 2.10 by σ^2 and Eq. 2.8 by $k_B T_i$, then adding the resulting equations, it can be seen that $\partial(\sigma^2 k_B T_i)/\partial t = 0$. This implies $\sigma^2 T_i = \text{constant}$, which is expected during adiabatic cooling of a UNP. Similarly, it can be shown that $\sigma^2 T_e = \text{constant}$. Combining Eqs. 2.8-2.11 implies that the total energy of the plasma,

$$E_{tot} = N_i \left\{ \frac{3}{2}(k_B T_e + k_B T_i) + \frac{3}{2} m_i \gamma^2 \sigma^2 \right\}, \quad (2.12)$$

is conserved during expansion.

Finally, solving Eqs. 2.8-2.11 determines the evolution of the size of the plasma cloud, the expansion velocity, $u(\mathbf{r}, t) = \gamma(t)\mathbf{r}$, and the ion and electron temperatures:

$$\sigma^2(t) = \sigma^2(0) \left(1 + \frac{t^2}{\tau_{exp}^2} \right), \quad (2.13)$$

$$\gamma(t) = \frac{t/\tau_{exp}^2}{1 + t^2/\tau_{exp}^2}, \quad (2.14)$$

$$T_\alpha(t) = \frac{T_\alpha(0)}{1 + t^2/\tau_{exp}^2}, \quad (2.15)$$

where the expansion rate is determined by the characteristic expansion time

$$\tau_{exp} = \sqrt{\frac{m_i \sigma(0)^2}{k_B [T_e(0) + T_i(0)]}}. \quad (2.16)$$

The value of τ_{exp} is approximately equal to 14 μs for our strontium plasma for a

typical initial size $\sigma(0) = 1$ mm, initial electron temperature, $T_e(0) = 50$ K, and initial ion temperature, $T_i(0) = 1$ K.

The expression for $\sigma(t)$ above (Eq. 2.13) shows how the plasma maintains a Gaussian profile during expansion. Equation 2.14 shows that the expansion velocity of ions ($\mathbf{u}(\mathbf{r}, t) = \gamma(t)\mathbf{r}$) is not only proportional to the position from the center, it is also proportional to time, as long as $t < \tau_{exp}$. On the other hand, as time increases and $t > \tau_{exp}$, then $\gamma(t) \approx 1/t$, signifying that acceleration decreases and the expansion velocity approaches a limit. Lastly, equation 2.15 shows adiabatic cooling of the thermal temperature of the ions and electrons. The experimental verification of equations 2.13-2.15 in ultracold plasmas was shown in,³⁴ with the exception of adiabatic cooling of the ions (Eq. 2.15 with $\alpha = i$).

It is important to notice that τ_{exp} dictates the evolution and expansion of the plasma and, as can be seen from 2.16, is completely determined by the initial conditions. We have assumed no dependence on radius for either electron or ion temperatures. However, in section 2.2.1, the temperature of the ions is shown to depend on interparticle distance, a , and therefore on density. Since the density profile of the plasma is Gaussian, this results in dependence of ion temperature on radius or distance from the plasma center. The characteristic expansion time, τ_{exp} , depends on both $T_e(0)$ and $T_i(0)$, but since $T_e(0) \gg T_i(0)$, small corrections coming from radial dependence do not affect the expansion.

2.2.4 Other physical processes

We have excluded in previous sections any collisional effects in the plasma. Depending on the specific processes, these will either heat or cool the plasma. Several of these have been studied extensively such as three-body recombination (TBR),^{46,29,11,31,47,48,39} Rydberg-electron collisions^{11,31} and ion-electron equilibration.¹² Gupta *et al.*¹⁴ show that when the initial $\Gamma_e < 0.2$, these processes are negligible and the dominant effects are DIH, KEO, and adiabatic cooling. When these processes are important ($\Gamma_e > 0.2$), the Vlasov equations are no longer applicable.

As we have seen, the physical processes that dominate the dynamics in ultracold plasmas vary both in their time scales and complexity. Studying these processes in UNPs will help to understand similar physics in other systems where measurements are not possible. The next chapter is devoted to explaining how measurements are performed in strontium ultracold neutral plasmas.

Chapter 3

Annular analysis of sheet fluorescence spectroscopy

3.1 Sheet fluorescence

Alkaline-earth elements such as strontium or calcium have the advantage of having their transitions at laser wavelengths that allow these atoms to be cooled and photoionized to form ultracold plasmas. Furthermore, the ionized version of alkaline-earth atoms have an electronic structure similar to alkali atoms, with, once again, convenient transitions at wavelengths that can be used for optical diagnostics.

The first optical diagnostic used on ultracold plasmas was absorption imaging of strontium ions performed by Simien *et al.*⁴ to study expansion. The absorption probe was henceforth utilized to study disorder-induced heating and Debye screening,²⁵ kinetic energy oscillations,^{25,26} and electron dynamics.¹⁴ Absorption spectroscopy is a great probe for studying plasmas as it can measure, accurately and without calibration, the number, density, and total kinetic energy of the ions in the plasma. However, since absorption measures total kinetic energy, *i.e.* expansion plus thermal energy, it is not well suited to measure ion temperature and its evolution. This is due to the fact that within a few microseconds after plasma creation, the thermal energy of the ions becomes negligible compared to their expansion energy, making it hard to extract temperature measurements from absorption spectra. Additionally,

absorption imaging measurements are always integrated through the entire plasma along the direction of propagation of the beam. This can be a big problem if the density profile of the plasma is not constant, as in the case of the Gaussian density profile of UNPs. As a result, absorption measurements in UNPs are density integrated measurements along the direction of propagation of the absorption beam.

Fluorescence imaging, on the other hand, is able to circumvent some of these shortcomings. Cummings *et al.*⁵ first used fluorescence in an ultracold neutral plasma of calcium. Plasma expansion parameters were extracted from the fluorescence scattered from a laser beam focused in a small region of the plasma. Fluorescence from strontium plasmas was later used by Laha *et al.*^{49,41} to study ion dynamics. Compared to absorption imaging on strontium ultracold plasmas, fluorescence imaging proved to have better signal-to-noise ratio as well as a shorter duty cycle for the experiment. Here I will describe a more general excitation and detection configuration as well as improvements in this technique that can better extract important parameters in strontium ultracold plasmas.

Figure 3.1 shows a schematic of the fluorescence imaging probe. The plasma is illuminated along the \hat{y} direction with a laser beam that is nearly resonant with the $^2S_{1/2} - ^2P_{1/2}$ transition in Sr^+ at $\lambda = 422$ nm (see Fig. 2.2). Fluorescence is recorded by the camera in a direction perpendicular to the probe beam ($-\hat{z}$). The intensity and duration of the fluorescence beam is low enough, that the ions typically scatter fewer than one photon during the time the beam is on, preventing any optical pumping to

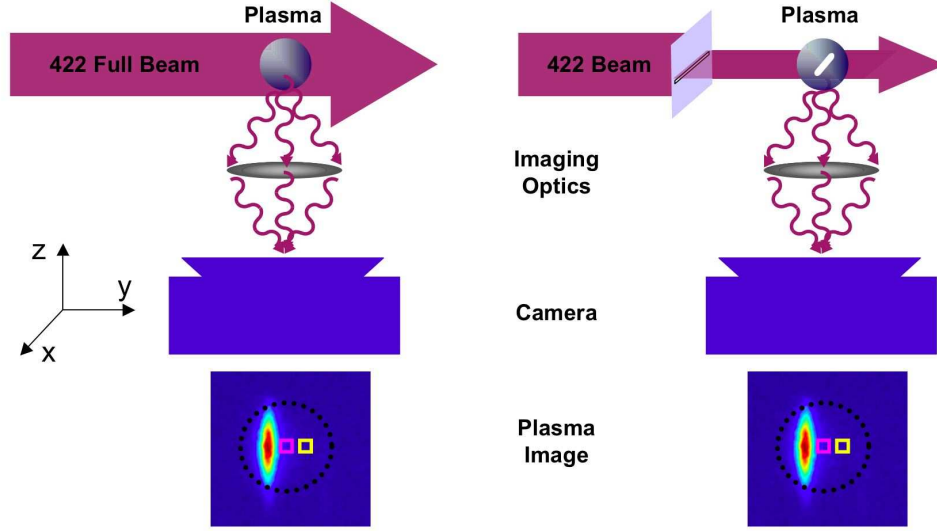


Figure 3.1 : Fluorescence probe for UNPs using light resonant with the main transition of Sr^+ . The laser beam propagates perpendicularly to a CCD intensified camera and the imaging axis. The images obtained in the camera are an $x - y$ projection of the fluorescing volume within the plasma. The fluorescence excitation beam can be spatially narrowed into a sheet. In this manner, the beam interacts with a smaller volume of the plasma where density variation is small. This smaller volume is represented in the figure by a small cylinder in the center of the plasma.

the metastable $^2D_{3/2}$ state.

The spatially-resolved fluorescence signal, $F(\nu, x, y)$, at laser frequency, ν , can be mathematically described by a convolution of a Lorentzian homogeneous width and an exponential for Doppler broadening, *i.e.* the probability for an ion to be in the excited state. This is then integrated over the density of the plasma and the intensity pattern of the fluorescence beam along the line of sight of the camera to obtain:

$$F(\nu, x, y) = C \frac{\gamma_0}{2} \int dz n_i(\mathbf{r}) \frac{I(x, z)}{I_{sat}} \int ds \frac{\gamma_0 / \gamma_{eff}}{1 + \left[\frac{2(\nu - s)}{\gamma_{eff} / 2\pi} \right]^2} \times \frac{1}{\sqrt{2\pi}\sigma_D[T_i(\mathbf{r})]} \exp \left\{ - \frac{[s - (\nu_0 + \nu_{exp}^y(\mathbf{r}))]^2}{2\sigma_D^2[T_i(\mathbf{r})]} \right\}. \quad (3.1)$$

The multiplicative factor, C , accounts for the collection solid angle, dipole radiation

pattern orientation, and detector efficiency. $n_i(\mathbf{r})$ is the ion density and $\gamma_{eff} = \gamma_0 + \gamma_{ins}$ is the effective Lorentzian linewidth due to the natural linewidth of the transition, $\gamma_0 = 2\pi \times 20$ MHz, and any instrumental linewidth, γ_{ins} . The intensity profile of the fluorescence excitation beam is $I(x, z)$ and, as mentioned above, we assume $I(x, z) \ll I_{sat} = 114$ mW/cm², the saturation intensity with linearly-polarized light, where the Clebsch-Gordon coefficients for the transition have been taken into account. The conventional Doppler width is $\sigma_D [T_i(\mathbf{r})] = (1/\lambda) \sqrt{k_B T_i(\mathbf{r}) / m_i}$ and the average resonance frequency of the transition for ions is Doppler-shifted from the resonance frequency, ν_0 , due to plasma expansion, $\nu_{exp}^y(\mathbf{r}) = \mathbf{u}(\mathbf{r}) \cdot \mathbf{k}$.

One can obtain quantitative information on ion density by performing fluorescence spectroscopy. This involves taking a series of camera exposures at equally spaced frequencies covering the entire ion resonance. There are many different ways to use this data, depending on the quantity of interest. If one is interested in getting signals proportional to the total number of ions in a region, one first integrates (or in reality, sums) over the frequency interval, to obtain the spatially resolved quantity:

$$\int d\nu F(\nu, x, y) = C \frac{\gamma_0^2}{8} \int dz n_i(\mathbf{r}) \frac{I(x, z)}{I_{sat}}. \quad (3.2)$$

If one is interested in the plasma as a whole, then integrating over the whole cloud yields,

$$\int d\nu \int dx dy F(\nu, x, y) = C \frac{\gamma_0^2}{8} \int dx dy dz n_i(\mathbf{r}) \frac{I(x, z)}{I_{sat}}. \quad (3.3)$$

Finally, if the laser intensity pattern is much larger than the plasma, one can assume

the intensity to be constant, resulting in

$$\int d\nu \int dx dy F(\nu, x, y) \approx C \frac{\gamma_0^2 I(0)}{8 I_{sat}} N_i. \quad (3.4)$$

This signal will be proportional to the total number of ions in the whole cloud, N_i . Calibrating this signal with absorption images determines the prefactor C , allowing the number of ions in the plasma to be extracted from the signal.

Following the procedure above, if one is interested in an $x - y$ region of interest, the expression to obtain the number of ions in that region is

$$\begin{aligned} \int d\nu \int_{x_1}^{x_2} \int_{y_1}^{y_2} dx dy F(\nu, x, y) &= C \frac{\gamma_0^2 I(0)}{8 I_{sat}} \int_{-\infty}^{\infty} dz \int_{x_1}^{x_2} \int_{y_1}^{y_2} dx dy n_i(\mathbf{r}) \\ &= C \frac{\gamma_0^2 I(0)}{8 I_{sat}} N_{i,region}. \end{aligned} \quad (3.5)$$

The equations above (3.1-3.5) show one of the drawbacks of fluorescence imaging. Just as in absorption imaging, the fluorescence signal is integrated over the \hat{z} direction; therefore every physical parameter obtain thus is averaged along that direction. To overcome this averaging, the fluorescence excitation beam can be spatially narrowed into a sheet,⁵⁰ as is shown in Fig. 3.1. This allows a very small region of the plasma to interact with the fluorescence beam, resulting in less averaging along the \hat{z} direction and a localized analysis of the small volume of the plasma where the density variation is also small. We call this method sheet fluorescence.

As light travels through the slit it will diffract. However, we saw that the diffraction effects were small for the size of the slits used (~ 1 mm) and the distance from slit to plasma (~ 1 m).

We align the sheet so it is centered on the plasma, so performing an integral similar to Eqs. 3.3 and 3.5, the total number of ions within the sheet ($N_{i,sheet}$) can be obtained:

$$\begin{aligned} \int d\nu \int dx dy F(\nu, x, y) &= C \frac{\gamma_0^2}{8} \int_{-z_0}^{z_0} dz \int dx dy n_i(\mathbf{r}) \frac{I(x, z)}{I_{sat}} \\ &\approx C \frac{\gamma_0^2}{8} \frac{I(0)}{I_{sat}} N_{i,sheet}, \end{aligned} \quad (3.6)$$

where the z integral extends over $2z_0$, the width of the fluorescence sheet.

Sheet fluorescence signals can also be analyzed in regions, to obtain an expression similar to 3.5:

$$\begin{aligned} \int d\nu \int dx dy F(\nu, x, y) &\approx C \frac{\gamma_0^2}{8} \frac{I(0)}{I_{sat}} \int_{-z_0}^{z_0} dz \int_{x_1}^{x_2} \int_{y_1}^{y_2} dx dy n_i(\mathbf{r}) \\ &\approx C \frac{\gamma_0^2}{8} \frac{I(0)}{I_{sat}} N_{i,sheet,region}, \end{aligned} \quad (3.7)$$

where now the region is also restricted along the z axis.

Equations 3.3-3.7 neglect the spatial variation of the excitation beam. If the laser spatial profile is Gaussian, but its finite size cannot be neglected, the measurement of the plasma width along the \hat{x} -axis will be distorted and the beam will not illuminate all ions equally along the \hat{z} -axis. With knowledge of the laser waist size, w , the effect can be accounted for.⁴¹ Calculating the total sheet fluorescence, we obtain,

$$\begin{aligned} \int d\nu \int dx dy F(\nu, x, y) &= C \frac{\gamma_0^2}{8} \int_{-z_0}^{z_0} dz \int dx dy \frac{I(0)}{I_{sat}} \exp\left(-\frac{2x^2 + 2z^2}{w^2}\right) \times \\ &\quad n_0 \exp\left(-\frac{x^2 + y^2 + z^2}{2\sigma(t)^2}\right) \end{aligned}$$

$$= C \frac{\gamma_0^2 I(0)}{8 I_{sat}} N_{i,sheet} \frac{w^2}{w^2 + 4\sigma(t)^2}. \quad (3.8)$$

Sheet fluorescence spectroscopy can also provide information about the temperature and expansion velocity of the plasma. We perform spatially resolved spectroscopy by summing the fluorescence signal given by Eq. 3.1 over a small area $\Delta x \Delta y$ in the $x - y$ image plane. The spectrum in that region will then be given by

$$\begin{aligned} S_{reg}(\nu) &= \int_{x_1}^{x_2} \int_{y_1}^{y_2} dx dy F(\nu, x, y) \\ &= C \frac{\gamma_0}{2} \int_{x_1}^{x_2} \int_{y_1}^{y_2} \int_{-z_0}^{z_0} dx dy dz \frac{n_i(x, y, z)}{\sqrt{2\pi\sigma_D[T_i(x, y, z)]}} \frac{I_0}{I_{sat}} \exp\left(-\frac{2x^2 + 2z^2}{w^2}\right) \times \\ &\quad \int_{-\infty}^{\infty} ds \frac{\gamma_0/\gamma_{eff}}{1 + \left[\frac{2(\nu-s)}{\gamma_{eff}/2\pi}\right]^2} \times \exp\left\{-\frac{[s - (\nu_0 + \nu_{exp}^y(\mathbf{r}))]^2}{2\sigma_D^2[T_i(x, y, z)]}\right\} \\ &\approx C \frac{\gamma_0}{8} \frac{I_0}{I_{sat}} N_{i,sheet,region} \frac{w^2}{w^2 + \sigma^2} \frac{1}{\sqrt{2\pi\sigma_D[T_i(\tilde{x}, \tilde{y}, \tilde{z})]}} \times \\ &\quad \int_{-\infty}^{\infty} ds \frac{\gamma_0/\gamma_{eff}}{1 + \left[\frac{2(\nu-s)}{\gamma_{eff}/2\pi}\right]^2} \exp\left\{-\frac{[s - (\nu_0 + \nu_{exp}^y(\mathbf{r}))]^2}{2\sigma_D^2[T_i(\tilde{x}, \tilde{y}, \tilde{z})]}\right\}, \end{aligned} \quad (3.9)$$

where $\tilde{x} = (x_2 - x_1)/2$, $\tilde{y} = (y_2 - y_1)/2$, and $\tilde{z} = 0$.

If Δx and Δy are small compared to the size of the plasma, the density, temperature, and expansion velocity can be taken as constant over the region. It was shown by Laha⁴¹ that this approximation is valid for $\Delta\alpha/\sigma < 0.25$, where $\alpha = x$ or y . In our analysis, we always keep $\Delta\alpha/\sigma < 0.25$ and so

$$S_{reg}(\nu) \propto \frac{I_0 N_{i,sheet,region}}{\sqrt{2\pi\sigma_D[T_i(\tilde{x}, \tilde{y}, \tilde{z})]}} \int_{-\infty}^{\infty} ds \frac{\gamma_0/\gamma_{eff}}{1 + \left[\frac{2(\nu-s)}{\gamma_{eff}/2\pi}\right]^2} \exp\left\{-\frac{[s - (\nu_0 + \nu_{exp}^y(\mathbf{r}))]^2}{2\sigma_D^2[T_i(\tilde{x}, \tilde{y}, \tilde{z})]}\right\}. \quad (3.10)$$

As we can see from 3.10, the fluorescence spectrum of a small region is given by a Voigt profile. This profile is Doppler shifted by an amount $\nu_{exp}^y(\mathbf{r}) = \mathbf{u}(\mathbf{r}) \cdot \mathbf{k}$ and

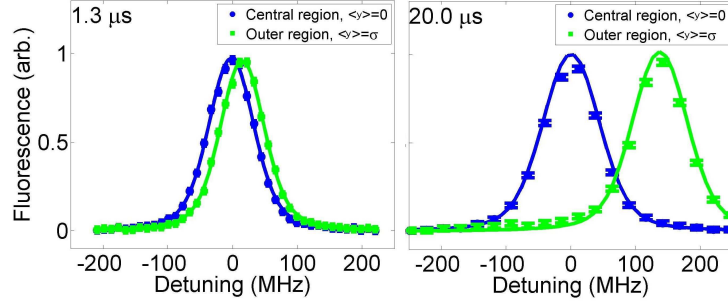


Figure 3.2 : Fluorescence spectra of two restricted regions of the plasma cloud showing the separation of expansion and random thermal motion effects. The plots show both regional spectra at different times after plasma formation (time shown on the upper left corner). Both spectra are normalized to their maximum values to make the comparison clear, in reality the outer region spectrum has a lower peak value. As the plasma expands the outer region spectrum shifts farther from $\nu = 0$. From the width of the spectra, one can extract a measurement of the ion thermal energy in each region of the plasma.

Doppler broadened, due to the average thermal energy at $x = \tilde{x}$, $y = \tilde{y}$, and $z = \tilde{z}$.

Fitting the spectrum to a Voigt profile, we will be able to extract the Doppler width, and through the relation $\sigma_D [T_i(\tilde{x}, \tilde{y}, \tilde{z})] = (1/\lambda) \sqrt{k_B T_i(\tilde{x}, \tilde{y}, \tilde{z})/m_i}$, the corresponding average temperature of the ions in that specific region.

Figure 3.2 illustrates the spectra from two different regions of the cloud; the central region and an outer region of the plasma. As time increases, the outer region spectrum shifts due to the expansion. On the other hand, the Doppler width in both spectra is only representative of thermal motion.

Figure 3.3 shows fluorescence measurements of the kinetic energy of the ions from two regions of the plasma, as well as measurements using the whole cloud image for analysis. Notice that in the whole cloud measurements, (inset 3.3) the kinetic energy surpasses the regional kinetic energy with values an order of magnitude higher. For

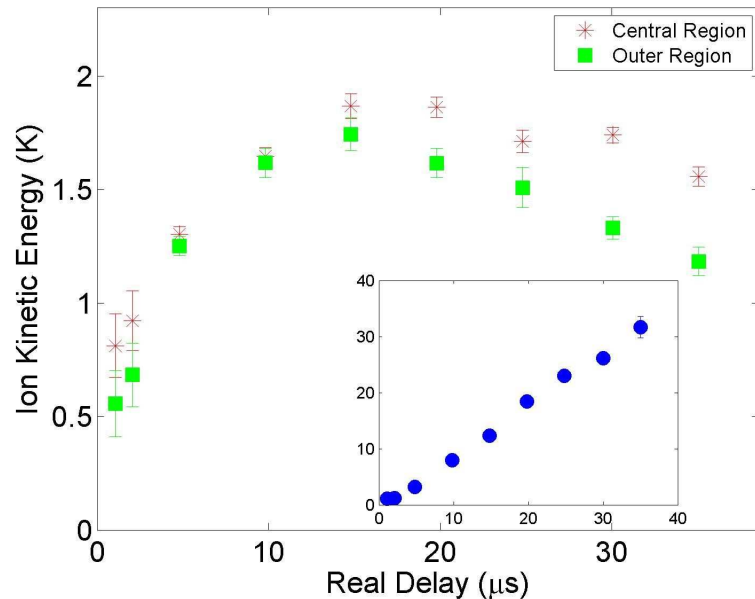


Figure 3.3 : Ion kinetic energy measurements done with regional analysis of fluorescence imaging. Both central and outer region measurements show the thermal energy of that particular region. Due to disorder-induced heating, the initial kinetic energy of the central region is higher than that of the outer region. The inset shows measurements done with whole cloud analysis where the expansion effect dominates because it cannot be decoupled. The initial conditions for these measurements are $T_e(0) = 48$ K, the peak ion density is $9 \times 10^{14} \text{ m}^{-3}$ and $\sigma_0 = 1.9$ mm.

the whole cloud measurement the approximation performed in 3.10 breaks down and the expansion energy dominates over the thermal energy.

It is in this decoupling of effects that one can notice the advantage of fluorescence imaging over absorption, as this type of measurement can separate expansion and thermal energy. A comparison of absorption, fluorescence, and fluorescence sheet measurement was shown by Castro *et al.*³⁷ Furthermore from sheet fluorescence measurements it is possible to obtain temperature information of regions in the plasma where the density variation is small and there is less averaging over density. This

opens the possibility of using sheet fluorescence to measure density dependent parameters (thermalization rate, oscillation frequency, etc) for ultracold plasmas. However, the analyzed regions are usually small, $< 0.25\sigma$, which results in a small signal-to-noise ratio. One could increase the size of the regions to increase the signal, but as the regions become larger so does the contribution of the expansion energy to the broadening of the spectra⁴¹ and the approximations made in Eq. 3.10 break down.

One can take advantage of the known symmetry of the Gaussian density profile and known expansion of the plasma to increase the signal-to-noise ratio without including expansion energy. Spherical Gaussian density implies that regions of the plasma located at the same radial distance have the same density and share the same plasma parameters. One could, in principle, combine all regions at constant radius into an annulus. We call this procedure annular analysis of fluorescence images and it is explained in the section that follows.

3.2 Description of annular analysis

As mentioned above, it is desirable to combine the signal from regions in the plasma that have the same density and same plasma parameters. In Eq. 3.10 the average resonance frequency from each region appears Doppler-shifted from the resonance frequency, ν_0 , due to plasma expansion. It is possible that different regions of plasma could experience different plasma expansion, and this would lead to different Doppler shifts. To be able to combine regions of the plasma, one has to understand the plasma

expansion and Doppler shift to adequately sum all contributions.

The Doppler shift in Eq. 3.10 can be explicitly written as $\nu_{exp}^y(\mathbf{r}) = \mathbf{u}(\mathbf{r}) \cdot \hat{y}/\lambda$, where $\mathbf{u}(\mathbf{r})$ is the expansion velocity and \mathbf{k} has been replaced by $\mathbf{k} = \hat{y}/\lambda$ (see Fig. 3.1). If the plasma is undergoing self-similar adiabatic expansion (see 2.2.3), the expansion velocity is given by Eq. 2.7 and the Doppler shift is then expressed as,

$$\nu_{exp}^y(\mathbf{r}) = \gamma(t) y/\lambda \quad (3.11)$$

where $\gamma(t)$ is given by Eq. 2.14. Equation 3.11 shows a correlation between the y coordinate in the plasma image and the Doppler shift ν_{exp}^y due to expansion. As a result of this correlation, regions in the plasma with different y locations have different Doppler shifts due to the expansion.

Consider now an annulus of width δr located at $r = \sqrt{x^2 + y^2}$. We can separate this annulus into small sections with their corresponding $\langle x \rangle$, $\langle y \rangle$ positions. Each of these sections will have different Doppler shifts by virtue of their different $\langle y \rangle$ positions. Adding the signal from all these sections, with different frequency shifts, would result in a broadening of the total spectrum of the annulus. In order to sum the contribution from distinct sections of an annulus, we first have to remove the frequency shift from each individual section.

To correctly account for the position of each individual annular section, it is necessary to calibrate the pixel size of our recorded images. Fluorescence images from the plasma are recorded by a CCD-intensified camera, where, as shown in Fig. 3.1, the images obtained are an $x - y$ projection of fluorescing plasma volume. A careful

measurement of the resolution of our fluorescence imaging system was performed to properly calibrate the pixel size of the camera (Appendix C). It was found that we are able to resolve features with a size of $12.4 \mu\text{m}$ and our pixel size corresponds to $13.14 \mu\text{m}$. With the proper calibration of pixel size, we can now proceed to locate the coordinates, (x_c, y_c) , of the center of the spherically symmetric plasma.

Let's rewrite Eq. 3.2 more explicitly:

$$\int d\nu F(\nu, x, y) = C \frac{\gamma_0^2}{8} \int_{-z_0}^{z_0} dz \frac{I(0)}{I_{sat}} \exp\left(-\frac{2(x-x_c)^2 + 2z^2}{w^2}\right) \times n_0 \exp\left(-\frac{(x-x_c)^2 + (y-y_c)^2 + z^2}{2\sigma(t)^2}\right). \quad (3.12)$$

Integrating over that whole spectrum would directly map the density of the plasma in a convolution with the Gaussian profile of the beam. To perform the integration in Eq. 3.12, we actually sum over all the fluorescence measurements performed at different frequencies, $S(x, y) = \int d\nu F(\nu, x, y) \rightarrow S(x_j, y_k) = \sum F(\nu_i, x_j, y_k)$, where x_j and y_k are the coordinates of individual pixels in the image for all the images recorded at different frequency ν_i . We then fit the sum of all the spectral images to a Gaussian and extract the plasma center coordinates.

It must be noted that in order for Eq. 3.12 to be valid, a plasma spectrum needs to be recorded with a wide enough frequency range to cover the entire ion resonance, *i. e.* $\nu_{min} \rightarrow -\infty$ and $\nu_{max} \rightarrow +\infty$. Experimentally this translates to measuring a wide enough spectrum that contains the wings of the Voigt profile. The results and data shown in this thesis were all taken within this condition and therefore Eq. 3.12

is valid. However, this is not always possible under certain experimental conditions, where other methods for finding the center need to be implemented. These include: performing approximations to Eq. 3.12, assigning as center coordinate the location of the maximum of $\int d\nu F(\nu, x, y)$, or using the center of the image taken with the fluorescence beam on resonance $F(\nu = \nu_0, x, y)$.

Once the location of the plasma center, (x_c, y_c) , is known, it is straightforward to properly assign the y position of each region in the plasma. To calculate the Doppler shift, all that remains is obtaining $\gamma(t)$. As can be seen from Eqs. 2.13 - 2.16, self similar expansion in ultracold plasmas only depends upon initial conditions, $\sigma(0)$, $T_e(0)$, and $T_i(0)$. These initial conditions are parameters that are under experimental control: $\sigma(0)$, the initial plasma size corresponds to the size of the trapped atom cloud just before ionization, $T_e(0)$ is set by the frequency of the photoionizing laser, and finally $T_i(0)$ can be calculated by using Eq. 2.1. We can then calculate $\gamma(t)$ and the average Doppler shift for every region during expansion.

Knowing v_{exp}^y , we can now transform the signal $F(\nu, x, y, t)$ to $F(\nu', x, y, t)$, where $\nu' = \nu - v_{exp}^y = \nu - \gamma(t)(y - y_c)/\lambda$. This “new” frequency, ν' , is shifted by the average Doppler shift due to expansion for that region, thus removing the effects of expansion.

In practice, the “new” frequency, ν' , is assigned to discrete frequency bins, where the bin resolution is made equivalent to the experimental resolution in frequency.

We can now construct the total fluorescence spectrum of an annulus by calculating,

$$S_{annulus}(\nu', t) = \int_{annulus} dx dy F(\nu', x, y, t). \text{ To do this integral, we sum over the pixels}$$

of the image that correspond to the annulus:

$$S_{annulus}(\nu'_i, t) \propto \sum \sum F(\nu'_i, x_j, y_k, t)$$

for x_j and y_k such that $r_{min} < \sqrt{(x_j - x_c)^2 + (y_k - y_c)^2} < r_{max}$. Here, r_{max} and r_{min} correspond to the outer and inner radius of the annulus located at $\tilde{r} = (r_{max} - r_{min})/2$ from the center and ν'_i corresponds to a particular frequency bin.

Let us demonstrate the process and benefits of annular analysis of sheet fluorescence. Figure 3.4 shows a sheet fluorescence image along with the schematic outline of an annulus. The image corresponds to $\nu \neq \nu_0$, and due to the correlation of y position and Doppler shift, the fluorescence maximum is not located on the center of the image. For illustrative purposes the annular analysis procedure is shown for four sections of the annulus (a, b, c, d). Sections b and c are located at $(\langle x_{b,c} \rangle \neq 0, \langle y_{b,c} \rangle = 0)$. Their corresponding spectra are thus centered about $\nu = 0$. Sections a and d on the other hand, are located at $(\langle x_{a,d} \rangle = 0, \langle y_{a,d} \rangle \neq 0)$ and their spectra are shifted from $\nu = 0$. Finally Fig. 3.4 shows all four spectra after the subtraction process. All spectra appear centered and can be added to obtain the total annular spectrum.

As a result of annular analysis, $S_{annulus}(\nu', t)$ is now centered about $\nu = 0$ and can be fitted to Voigt profile to obtain the Doppler width of the spectrum, σ_D . From here one can calculate the corresponding average temperature of the ions in the annulus, $T_{i,ave}(\tilde{r}) = m_i(\sigma_D \lambda)^2 / k_B$.

Let us reiterate the process of constructing annular spectra. A plasma spectrum is taken by capturing a series of camera exposures (plasma fluorescence images) at

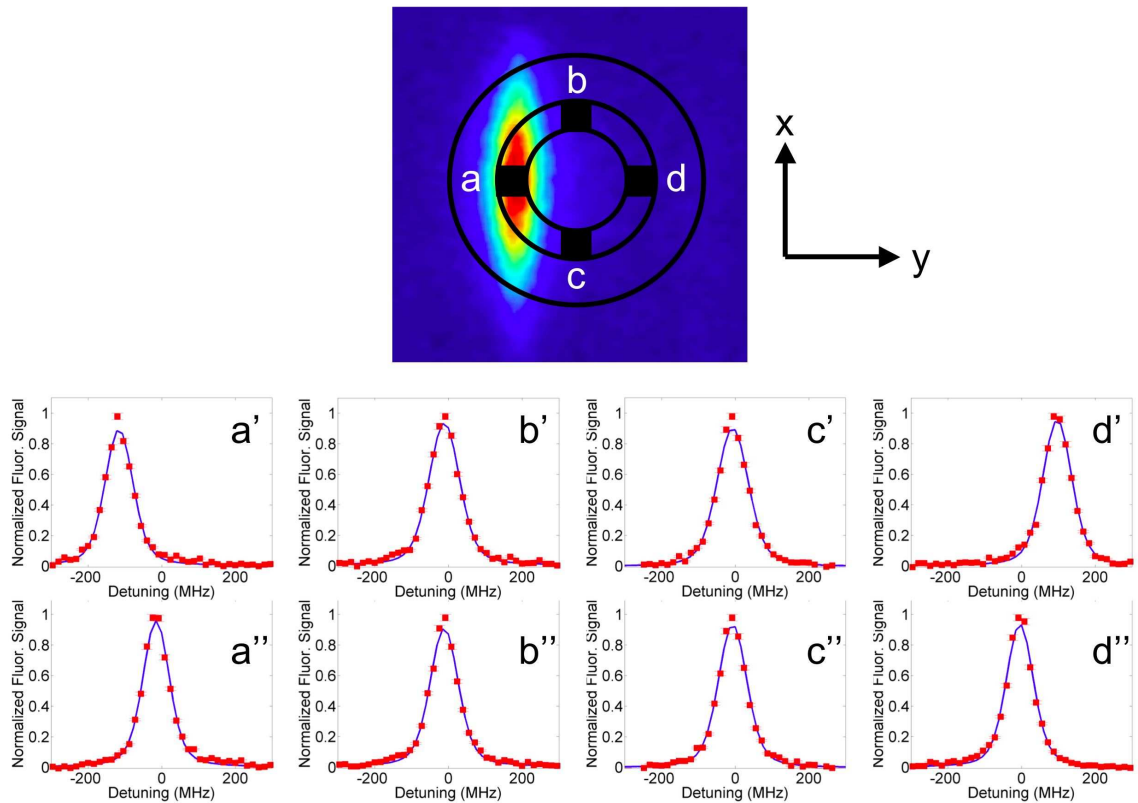


Figure 3.4 : Schematic to demonstrate the removal of the Doppler shift from distinct sections of an annulus. Shown above are four regions of an annulus (a, b, c, d) with the respective spectra (a', b', c', d'). Spectra b' and c' have no frequency shift since $\langle y \rangle = 0$ for these sections. In the final set of spectra (a'', b'', c'', d'') the Doppler shift from each region has been subtracted.

equally spaced laser frequencies covering the entire ion resonance. This means that each image taken corresponds to a different laser frequency, ν . The following procedure is then performed to every image:

1. Each pixel is assigned coordinates (x, y) centered about (x_c, y_c) .
2. Each pixel is placed in a particular annulus according to its location, $r_{min} < \sqrt{(x - x_c)^2 + (y - y_c)^2} < r_{max}$, where $r_{max} - r_{min}$ is the width of the annulus.
3. A new frequency is calculated for every pixel according to $\nu' = \nu - \gamma(t)(y - y_c)/\lambda$.
This frequency is placed in the appropriate frequency bin.
4. The signal from all the pixels of the annulus is then added together.

To obtain an accurate spectrum and measurement of $T_{i,ave}(\tilde{r})$ it is very important to check that the Doppler shift in frequency due to expansion is subtracted correctly. Any incorrect subtraction would result in broadening of the spectrum. The center of the plasma has to be well determined and the expansion of the plasma has to be properly estimated. To ensure the proper subtraction of the Doppler shift, several checks are performed during the analysis process.

The first of these checks consists of examining whether the plasma center was found correctly. If we have an incorrect value for y_c , the calculated Doppler shifts will be over or underestimated. In any case the contributions from different images to the annulus would not be properly shifted. To illustrate the results of having the wrong center coordinates, we analyze the data by artificially using the wrong center

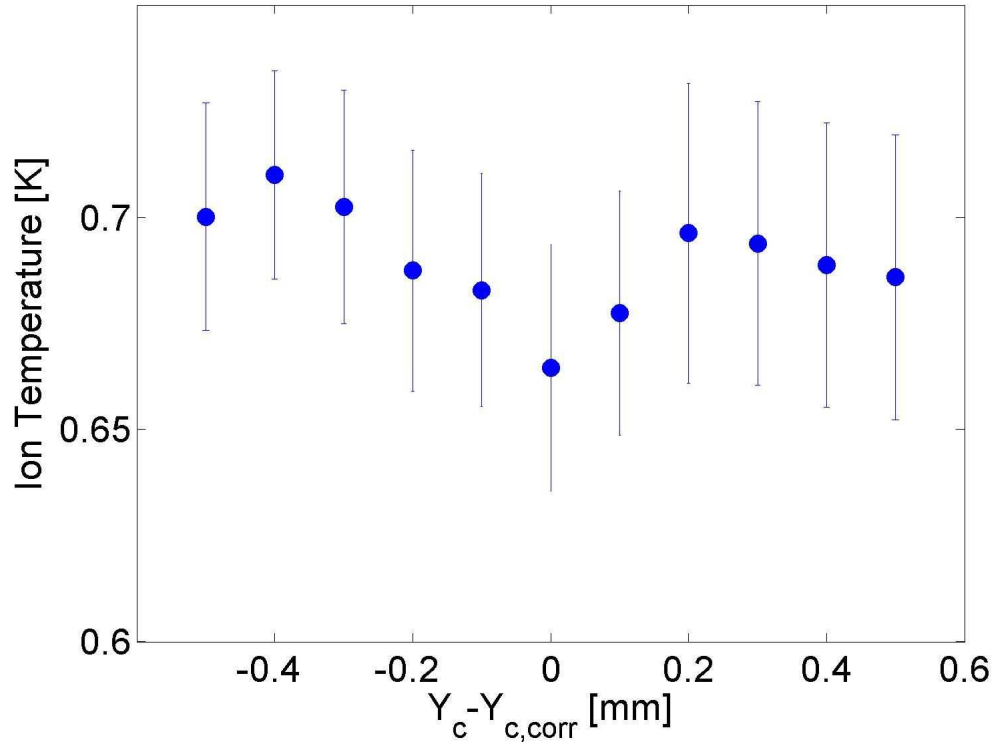


Figure 3.5 : Ion temperature versus $(y_c - y_{c,corr})$. The minimum, narrowest spectrum is found at the correct center coordinate, $y_{c,corr}$.

coordinates as an input. Plotting the temperature (linewidth)² versus the artificial y_c shows how the minimum temperature, corresponding to a narrower spectrum and correct subtraction, comes when the artificial center coordinate equals the actual, correct center coordinate (Fig. 3.5).

On the other hand, an incorrect x_c location will not have any effect on the Doppler shift, since the shift only depends on \hat{y} (the direction of laser propagation). However, the annulus located with an artificially incorrect x_c will be displaced and therefore will not have the symmetry of the Gaussian profile with resulting non-uniformity in density or temperature. Figure 3.6 shows how the linewidth is affected by artificially

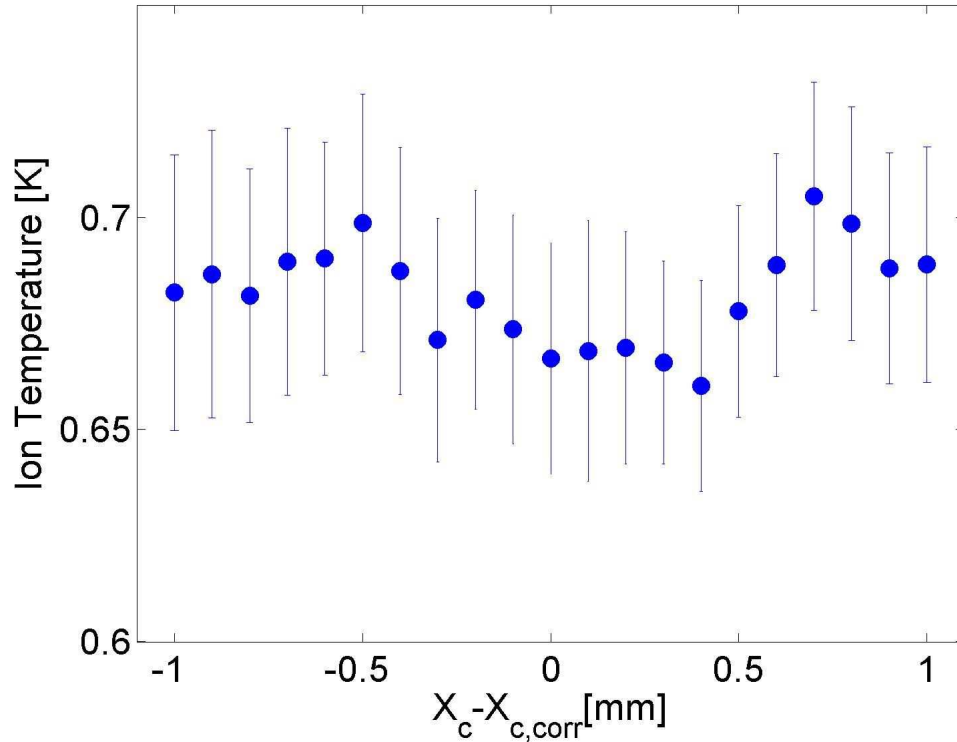


Figure 3.6 : Ion temperature versus $(x_c - x_{c,corr})$. The minimum, narrowest spectrum is found at the correct center coordinate, $x_{c,corr}$.

changing the x center coordinate.

Now if the expansion is not determined adequately, *i. e.* if $\sigma(0)$, $T_e(0)$ or $T_i(0)$ are not well known, the spectrum would appear skewed and broad. Once more, we analyze the data by artificially using an incorrect electron temperature as an input. Figure 3.7 displays the effect on the temperature (linewidth)² versus the artificially changed T_e , showing how the linewidth is affected by an incorrect calculation of the expansion (Fig. 3.6).

As mentioned above, figures such as 3.5-3.7 are generated and checked during the analysis to make sure the expansion is accurately subtracted. The correct center

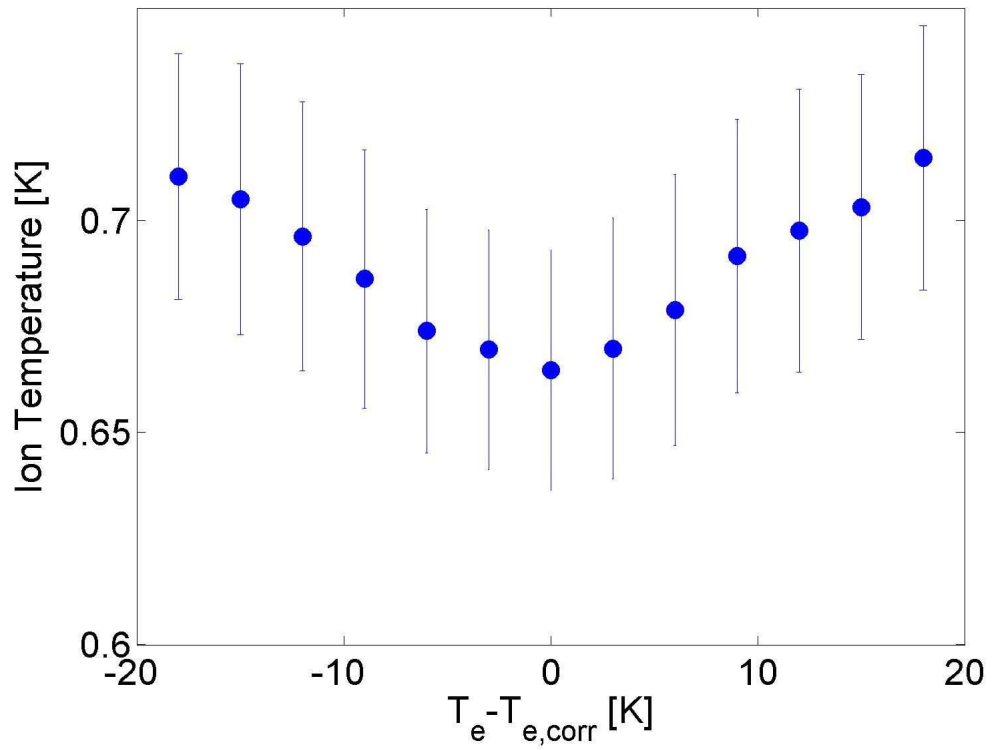


Figure 3.7 : Ion temperature versus $(T_e - T_{e,corr})$. The minimum, narrowest spectrum is found at the correct electron temperature, $T_{e,corr}$.

coordinates and expansion parameters will produce the narrowest (coldest) spectra. These figures can also give us a handle as to how uncertainties in the center coordinates or initial conditions of the plasma affect the measurements. From figure 3.5, not knowing y_c to within 0.4 mm (~ 31 pixels) about the correct coordinate, $y_{c,corr}$ would result in an error of $\sim 5\%$ in the ion temperature, T_i . On the other hand, not knowing x_c is more “forgiving” as we would obtain the same $\sim 5\%$ error in T_i , if the center was off by ~ 1.0 mm (~ 77 pixels) (see Fig. 3.6). Finally, figure 3.7 shows that an uncertainty of ± 10 K in T_e would result in $\sim 5\%$ error in T_i .

We must also address how the width of the annulus may affect our ability to remove expansion. Figure 3.8 shows how the resulting ion temperature, T_i , with corresponding spectrum linewidth, changes with the annular width. At large annular widths $> 0.25\sigma$, the expansion is not constant within the annulus and some expansion energy will then broaden the spectrum. At annular widths $< 0.20\sigma$, the signal-to-noise ratio is not high enough to result in a good temperature measurement. We can conclude that the optimum width is between 0.20σ and 0.25σ .

The chapter that follows shows an application of annular analysis of sheet fluorescence to a study of kinetic energy oscillations. Finally, I would like to close this chapter by mentioning that a copy of the MATLAB code that performs annular analysis of sheet fluorescence can be found in Appendix B.

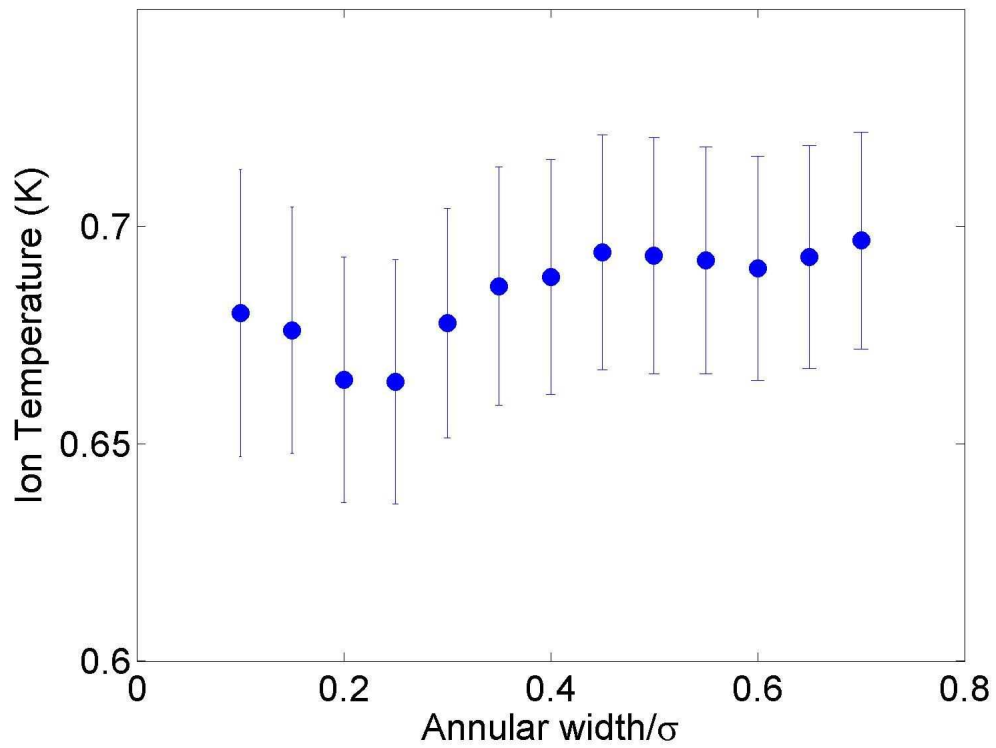


Figure 3.8 : Ion temperature versus annular width. At very low widths, the signal-to-noise ratio is not good enough, resulting in higher temperature. At higher values of the annular width the expansion is no longer constant within the annulus. The figure shows how the optimum width is 0.20σ to 0.25σ . The data in figures 4.1 and 4.2 was taken with an annular width of 0.25σ .

Chapter 4

Application of annular analysis to kinetic energy oscillation measurements

As mentioned in the previous chapter, annular analysis permits the study of regions with insignificant density variation. This is beneficial for studying density-dependent phenomena such as disorder-induced heating and kinetic energy oscillations mentioned in sections 2.2.1 and 2.2.2.

Figure 4.1 shows kinetic energy measurements performed with annular analysis of sheet fluorescence images, which has removed the Doppler shift due to expansion from the spectrum, leaving a pure measurement of ion thermal motion. It is seen in the figure how the initially uncorrelated ions heat up due to disorder-induced heating. The typical ion energy after equilibration is about $e^2/(4\pi\epsilon_0 a)$, which is on the order of 1 K of energy. The density dependence of this process can be readily seen in the figure. Annuli located closer to the center have higher density and will heat up to a higher temperature.

As mentioned before, the time scale for disorder-induced heating corresponds to the inverse of the ion plasma oscillation frequency, $1/\omega_{pi} = \sqrt{m_i\epsilon_0/(n_i e^2)}$, which is on the order of a few hundred nanoseconds. As the ions overshoot the minimum of their potential well, kinetic energy oscillations ensue. This oscillation frequency is also density-dependent, making annular analysis of sheet fluorescence an ideal tool to

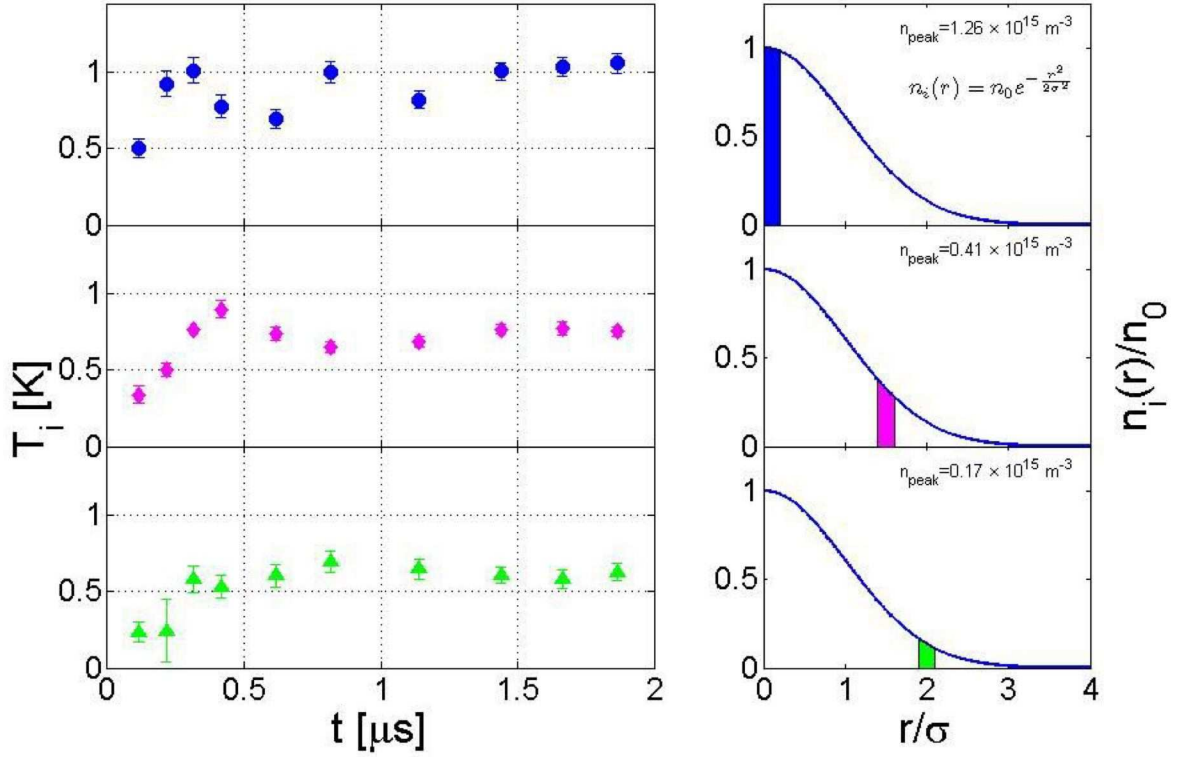


Figure 4.1 : Annular analysis of kinetic energy oscillations in an ultracold neutral plasma. As spatial correlations develop, ion potential energy is converted to kinetic energy. The kinetic energy oscillates about its equilibrium value with the plasma frequency, $\omega_{pi} \propto n^{1/2}$. An ultracold neutral plasma has a Gaussian density distribution, therefore the central annulus $\langle r \rangle = 0$ has higher density than any other annuli and oscillates faster. Notice how the oscillation frequency and the equilibrium energy value diminishes as $\langle r \rangle$ increases.

study this phenomenon.

Disorder-induced heating and kinetic energy oscillations are universal processes in strongly correlated plasmas that scale with density. Figure 4.2 shows a plot of DIH and KEO from Fig. 4.1 in which the thermal energy has been scaled by T_{DIH} and time has been scaled by ω_{pi} .

Figures 4.1 and 4.2 show a higher contrast of kinetic energy oscillation than ever seen before.^{25,26} This higher contrast is only possible due the removal of the effects of

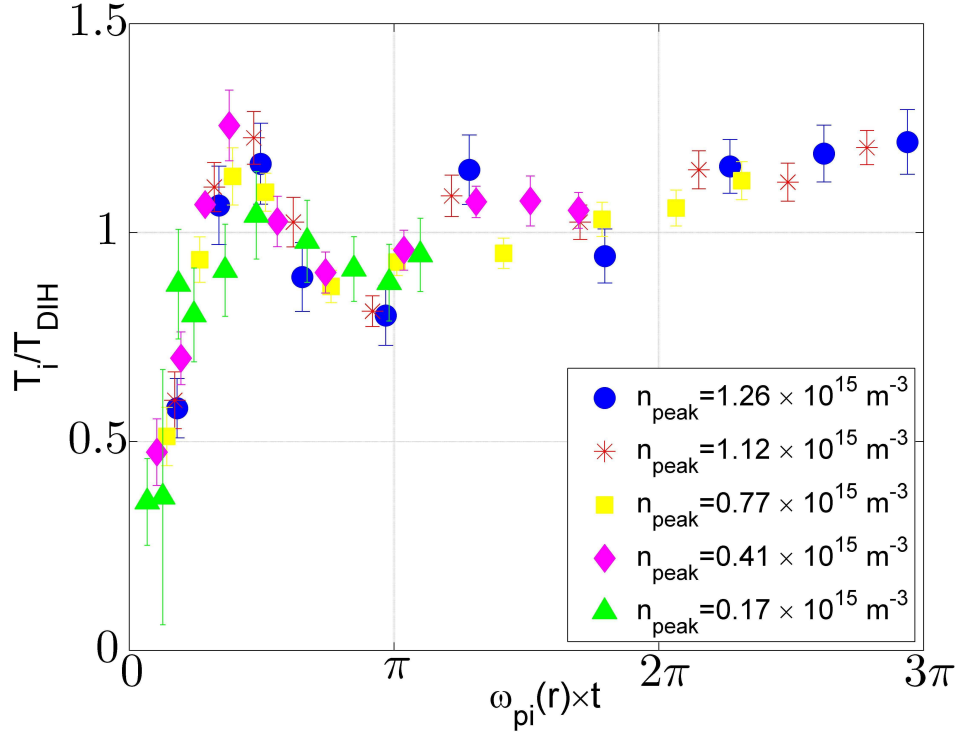


Figure 4.2 : Normalized kinetic energy oscillations of ultracold plasmas. T_{DIH} is the temperature obtained from eq. 2.1 and ω_{pi} is the ion plasma frequency. The different symbols correspond to different annuli in a strontium UNP. Due to their different location, they have different densities. T_{DIH} and ω_{pi} depend on density. Appropriately scaling temperature and time to these quantities creates a universal curve for disorder-induced heating and kinetic energy oscillations.

expansion velocity on the measurement and the higher signal-to-noise ratio obtained through annular analysis. Annular analysis is therefore an excellent tool for analyzing regions of the plasma without compromising signal-to-noise ratio and without introducing expansion energy to measurements of thermal energy.

Chapter 5

Conclusions

The objective of the work presented here was to develop the ability to study regions in an ultracold plasma with a small density distribution, while maximizing the signal-to-noise ratio. This thesis presents the implementation of experimental and computational techniques that improve the signal-to-noise ratio in fluorescence measurements in ultracold plasma experiments. To reduce the density variation, we performed sheet fluorescence measurements and regional analysis of those measurements. To increase the signal-to-noise ratio, it was necessary to add small regions of the plasma with similar density distributions into an annulus. To accomplish this task we developed a software analysis tool that removes the expansion energy and corresponding frequency shift from distinct sections of the aforementioned annulus before summing the signal together. Upon successful removal of the expansion energy, we have obtained a fluorescence signal with higher resolution.

Although it is a great tool for studying density dependent phenomena, annular analysis is limited to measurements where the plasma expansion is spherically or cylindrically symmetric. Even if the expansion is not exactly known, it is always possible to first perform measurements of the expansion velocity and then remove it appropriately.

The implementation of a non-invasive probe that permits measurements of re-

gions with small density variation is crucial in investigating density dependent strong-coupling effects in ultracold neutral plasmas, such as disorder-induced heating and kinetic energy oscillations.^{27,51} Furthermore, the development of annular analysis of fluorescence images will allow us to probe the temperature of UNPs at longer time scales, which will be crucial for future studies such as the adiabatic cooling of ions during expansion and the establishment of global ion thermal equilibrium and electron-ion thermalization.

Bibliography

- [1] Killian, T. C.; Pattard, T.; Pohl, T.; Rost, J. M. *Phys. Rep.* **2007**, *449*, 77.
- [2] Metcalf, H. J.; van der Straten, P. *Laser Cooling and Trapping*; Springer-Verlag: New York, New York, 1999.
- [3] Killian, T. C.; Kulin, S.; Bergeson, S. D.; Orozco, L. A.; Orzel, C.; Rolston, S. L. *Phys. Rev. Lett.* **1999**, *83*, 4776.
- [4] Simien, C. E.; Chen, Y. C.; Gupta, P.; Laha, S.; Martinez, Y. N.; Mickelson, P. G.; Nagel, S. B.; Killian, T. C. *Phys. Rev. Lett.* **2004**, *92*, 143001.
- [5] Cummings, E. A.; Daily, J. E.; Durfee, D. S.; Bergeson, S. D. *Phys. Rev. Lett.* **2005**, *95*, 235001.
- [6] Rolston, S. L.; Bergeson, S. D.; Kulin, S.; Orzel, C. *Bull. Am. Phys. Soc.* **1984**, *43*, 1324.
- [7] Robinson, M. P.; Tolra, B. L.; Noel, M. W.; Gallagher, T. F.; Pillet, P. *Phys. Rev. Lett.* **2000**, *85*, 4466.
- [8] Morrison, J. P.; Rennick, C. J.; Keller, J. S.; Grant, E. R. *Phys. Rev. Lett.* **2008**, *101*, 205005.
- [9] Ichimuru, S. *Rev. Mod. Phys.* **1982**, *54*, 1017.
- [10] Gericke, D. O.; Murillo, M. S. *Contrib. Plasma Phys.* **2003**, *43*, 298.

- [11] Robicheaux, F.; Hanson, J. D. *Phys. Plasmas* **2003**, *10*, 2217.
- [12] Kuzmin, S. G.; O'Neil, T. M. *Phys. Plasmas* **2002**, *9*, 3743.
- [13] Mazevet, S.; Collins, L. A.; Kress, J. D. *Phys. Rev. Lett.* **2002**, *88*, 55001.
- [14] Gupta, P.; Laha, S.; Simien, C. E.; Gao, H.; Castro, J.; Killian, T. C.; Pohl, T. *Phys. Rev. Lett.* **2007**, *99*, 75005.
- [15] Horn, H. M. V. *Science* **1991**, *252*, 384.
- [16] Morfill, G. E.; Thomas, H. M.; Konopka, U.; Zuzic, M. *Phys. Plasmas* **1999**, *6*, 1769.
- [17] Mitchell, T. B.; Bollinger, J. J.; Huang, X. P.; Itano, W. M.; Dubin, D. H. E. *Phys. Plasmas* **1999**, *6*, 1751.
- [18] Nantel, M.; Ma, G.; Gu, S.; Cote, C. Y.; Itatani, J.; Umstadter, D. *Phys. Rev. Lett.* **1998**, *80*, 4442.
- [19] Springate, E.; Hay, N.; Tisch, J. W. G.; Mason, M. B.; Ditmire, T.; Hutchinson, M. H. R.; Marangos, J. P. *Phys. Rev. A* **2000**, *61*, 063201.
- [20] Perry, M. D.; Mourou, G. *Science* **1994**, *264*, 917.
- [21] Lindl, J. *Phys. Plasmas* **1995**, *2*, 3933.
- [22] Clark, E. L.; Krushelnick, K.; Davies, J. R.; Zepf, M.; Tatarakis, M.; Beg, F. N.; Machacek, A.; Norreys, P. A.; Santala, M. I. K.; Watts, I.; Dangor, A. E. *Phys.*

- Rev. Lett.* **2000**, *84*, 670.
- [23] Snavely, R. A. et al. *Phys. Rev. Lett.* **2000**, *85*, 2945.
- [24] Killian, T. C. *Science* **2007**, *316*, 705.
- [25] Chen, Y. C.; Simien, C. E.; Laha, S.; Gupta, P.; Martinez, Y. N.; Mickelson, P. G.; Nagel, S. B.; Killian, T. C. *Phys. Rev. Lett.* **2004**, *93*, 265003.
- [26] Laha, S.; Chen, Y. C.; Gupta, P.; Simien, C. E.; Martinez, Y. N.; Mickelson, P. G.; Nagel, S. B.; Killian, T. C. *Euro. Phys. J. D* **2006**, *40*, 51.
- [27] Murillo, M. S. *Phys. Rev. Lett.* **2001**, *87*, 115003.
- [28] Kulin, S.; Killian, T. C.; Bergeson, S. D.; Rolston, S. L. *Phys. Rev. Lett.* **2000**, *85*, 318.
- [29] Killian, T. C.; Lim, M. J.; Kulin, S.; Dumke, R.; Bergeson, S. D.; Rolston, S. L. *Phys. Rev. Lett.* **2001**, *86*, 3759.
- [30] Robicheaux, F.; Hanson, J. D. *Phys. Rev. Lett.* **2002**, *88*, 55002.
- [31] Pohl, T.; Pattard, T.; Rost, J. M. *Phys. Rev. A* **2004**, *70*, 033416.
- [32] Pohl, T.; Pattard, T.; Rost, J. M. *Phys. Rev. Lett.* **2004**, *92*, 155003.
- [33] Cummings, E. A.; Daily, J. E.; Durfee, D. S.; Bergeson, S. D. *Phys. Plasmas* **2005**, *12*, 123501.

- [34] Laha, S.; Gupta, P.; Simien, C. E.; Gao, H.; Castro, J.; Killian, T. C. *Phys. Rev. Lett.* **2007**, *99*, 155001.
- [35] Roberts, J. L.; Fertig, C. D.; Lim, M. J.; Rolston, S. L. *Phys. Rev. Lett.* **2004**, *92*, 253003.
- [36] Nagel, S. B.; Simien, C. E.; Laha, S.; Gupta, P.; Ashoka, V. S.; Killian, T. C. *Phys. Rev. A* **2003**, *67*, 011401.
- [37] J. Castro, H. G.; Killian, T. C. *Journal of Plasma Physics and Controlled Fusion* **2008**, *50*, 124011.
- [38] Gupta, P. M.Sc. thesis, Rice University, 2004.
- [39] Kuzmin, S. G.; O'Neil, T. M. *Phys. Rev. Lett.* **2002**, *88*, 65003.
- [40] Hamaguchi, S.; Farouki, R. T.; Dubin, D. H. E. *Phys. Rev. E* **1997**, *56*, 4671.
- [41] Laha, S. Ph.D. thesis, Rice University, 2007.
- [42] Killian, T. C.; Chen, Y. C.; Gupta, P.; Laha, S.; Martinez, Y. N.; Mickelson, P. G.; Nagel, S. B.; Saenz, A. D.; Simien, C. E. *J. Phys. B: At. Mol. Opt. Phys.* **2005**, *38*, 351, (Equations 7, 10, 11, and 17 should be multiplied by γ_0/γ_{eff}).
- [43] Dorozhkina, D. S.; Semenov, V. E. *Phys. Rev. Lett.* **1998**, *81*, 2691.
- [44] Baitin, A. V.; Kuzanyan, K. M. *J. Plasma Phys.* **1998**, *59*, 83.

- [45] Mora, P. *Phys. Plasmas* **2005**, *12*, 112102.
- [46] Mansbach, P.; Keck, J. *Phys. Rev.* **1969**, *181*, 275.
- [47] Pohl, T.; Vrinceanu, D.; Sadeghpour, H. R. *Phys. Rev. Lett.* **2008**, *100*, 223201.
- [48] Hahn, Y. *Phys. Lett. A* **1997**, *231*, 82.
- [49] S. Laha, J. Castro, H. G. P. G. C. E. S.; Killian, T. C. 15th International Conference on Atomic Processes in Plasmas, 2007; p 69.
- [50] J. Castro, H. G.; Killian, T. C. 9th International Workshop on Non-Neutral Plasmas, 2008; p 3.
- [51] Zwicknagel, G. *Contrib. Plasma Phys.* **1999**, *39*, 155.
- [52] Gupta, P. Ph.D. thesis, Rice University, 2007.

Appendix A

Improvements in ionization fraction

As mentioned in chapter 2, we photoionize the atoms in our experiment with a two photon process. This process involves one laser pulse with its frequency tuned to the ($^1S_0 - ^1P_1$) transition of strontium at 461 nm, followed by a second laser pulse from a dye laser tuned just above the ionization continuum at ~ 412 nm. The fraction of trapped atoms that is ionized is then dependent on the number of excited atoms and the energy of the second photoionizing beam.

A general schematic of both these lasers is displayed in Fig. A.1. The Nd:YAG laser shown in the figure is used as a pump laser for a total of four dye cells. The Nd:YAG laser generates 10 ns pulses at 355 nm with a repetition rate of 10 Hz. The figure shows three dye cells inside an enclosure that generate and amplify light at 412 nm. This corresponds to the photoionizing beam. Figure A.1 also shows the fourth cell outside the enclosure. This cell will amplify a seed laser beam at 461 nm. Due to the pulsed nature of the Nd:YAG pump beam, all four dye cells generate 10 ns pulses as well.

Figure A.3 describes the photoexcitation beam setup in more detail. This was first implemented in our laboratory by Priya Gupta.^{38,52} This photoexcitation laser generates tunable light at 412 nm. To generate light of this frequency, this laser uses a dye molecule known as Exalite 411 in solution with P-Dioxane.

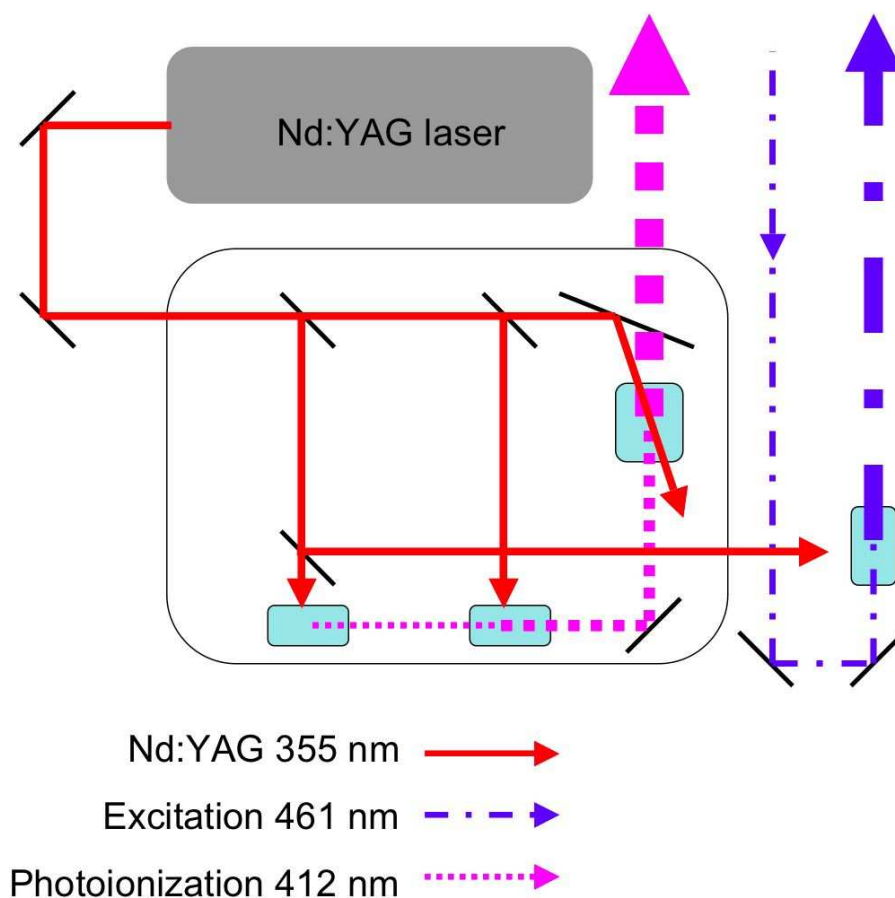


Figure A.1 : Pulsed dye laser setup for photoionization of strontium. The Nd:YAG laser is used as a pump laser and generates 10 ns pulses at 355 nm with a duty cycle of 10 Hz. These UV pulses excite the molecules in the dyes to excited states. The excited molecules will then lase at certain frequencies. Schematically shown in the enclosure, three dye cells generate and amplify the photoionizing beam at 412 nm. A final external cell amplifies a seed laser beam at 461 nm.

Three dye cells are used for this laser. The first cell generates pulsed light within a frequency range about 411 nm. A diffraction grating (not shown in the figure), selects the frequency of the beam that will lase in the oscillator cell. Frequency tuning of this laser can be accomplished by tilting the diffraction grating, changing the light's angle of incidence and thus changing the frequency. The tuned pulsed light generated in the oscillator cell is then amplified in dual stage preamplifier and amplifier cells.

Figure A.3 shows how both oscillator and preamplifier cells are pumped transversely by the Nd:YAG pulse, *i. e.* the pumped beam is perpendicular to the light produced or amplified in the dye cell. These cells contain the same concentration of Exalite 411 at 2.1×10^{-4} mol/L. The solution containing the dye circulates through both these cells by means of a *MICROPUMP* circulator, model 040 – 000 – 200. The solution flows with a speed of 0.69 L/min.

Contrary to the oscillator and preamplifier cells, the amplifier cell is longitudinally pumped as the Nd:YAG pulse is almost collinear with the 412 nm light. Compared to transverse pumping, longitudinal pumping enables a higher amplification of the beam. The concentration in this cell is different than that of the other two cells at 3.44×10^{-5} mol/L. As such, this amplifier cell has an independent circulating system. Improvements were made in the system by replacing the older *MICROPUMP* circulator, model 040 – 332, with a *Little Giant Pump* circulator, model 3-MD-MT-HC, with faster flow rate of 0.93 L/min. To further enhance this flow system the diameter of the tubing to the amplifier stage was increased from 1/4" to 5/8".

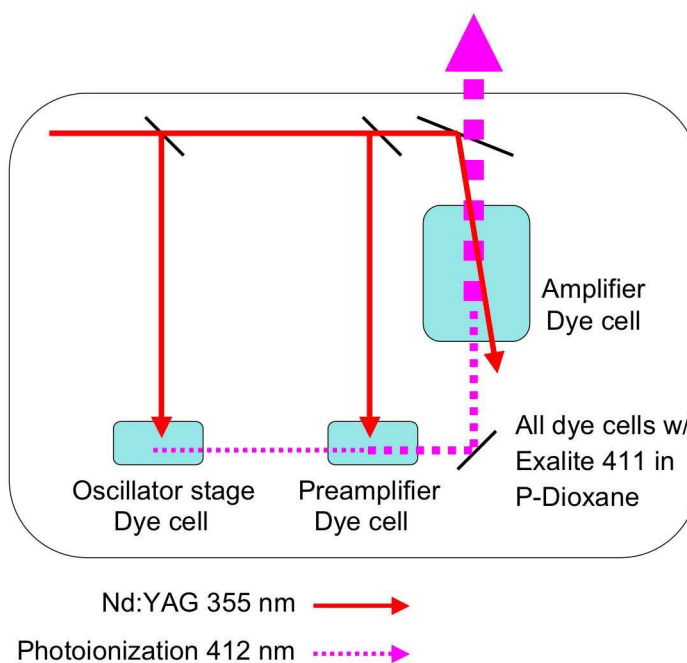


Figure A.2 : Pulsed dye laser setup for generating the ionizing beam. All three cells shown here used Exalite 411 in solution with P-Dioxane. The pulsed light generated in the oscillator cell is frequency selected by a diffraction grating (not shown) and amplified by a preamplifier and amplifier cell . As can be seen from the figure both oscillator and preamplifier cells are pumped transversely by the Nd:YAG pulse . On the other hand the amplifier cell is longitudinally pumped.

Further details of the development, tuning capabilities and calibration of this dye laser can be found in Priya Gupta's Master thesis and Ph. D. dissertation.^{38,52}

To conclude, the final improvement to the photoionization process was the addition of pulse-amplification of the excitation beam. Pulse-amplification of the beam results in an increase in the number of atoms in the excited state. A continuous laser beam at 461 nm is used as a seeding laser for this pulse-amplification. The beam travels through a glass cell contain the dye molecule Coumarin 460 in solution with Methanol at a concentration of 4.0×10^{-4} mol/L. The dye solution flows with a speed of 2.48

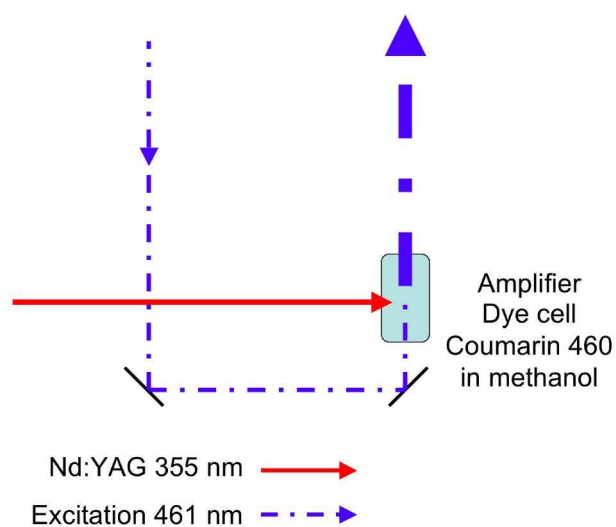


Figure A.3 : Pulsed dye laser setup. A seeding beam of 461 nm light travels through a glass cell containing a solution of methanol and Coumarin 460. This cell is transversely pumped by a 10 ns Nd:YAG pulse to produce pulse-amplification of the seed laser.

L/min. This cell is transversely pumped by the 10 ns pulsed Nd:YAG laser, resulting in amplification of 461 nm light in a 10 ns pulse. Figure A.3 shows a schematic of the pulse-amplification scheme.

Appendix B

MATLAB code for annular analysis

The MATLAB code for performing annular analysis can be found can be found in

<http://www.owl.net.rice.edu/~killian/research.shtml>.

Appendix C

Calibration of imaging resolution

In order to locate and properly remove the Doppler shift due to expansion, it was necessary to properly calibrate our imaging system.

Figure C.1 shows the optical layout of our imaging system. The figure traces the path of both the absorption and fluorescence beams. We use both imaging techniques as they complement each other (see Chapter 3).

In order to calibrate this imaging system the USAF 1951 resolution target was placed in the middle of the vacuum chamber at the location of the plasma. Figure C.2 shows the placement of the target with respect to the lenses. The figure schematically shows how a translation stage was placed on one of the imaging lenses in order to optimize our resolution. The resolution target was also placed on a translation stage to be able to map out the resolution in different positions centered about the location of the plasma.

Figure C.2 also shows an image of the resolution target used. To measure the resolution of our imaging system the absorption imaging beam was used on the resolution target. The target will cast a shadow on the camera and images of the target were recorded.

The resolution is measured by the ability to resolve line pairs within the target. The target is separated into groups, which in turn are separated into elements. Each

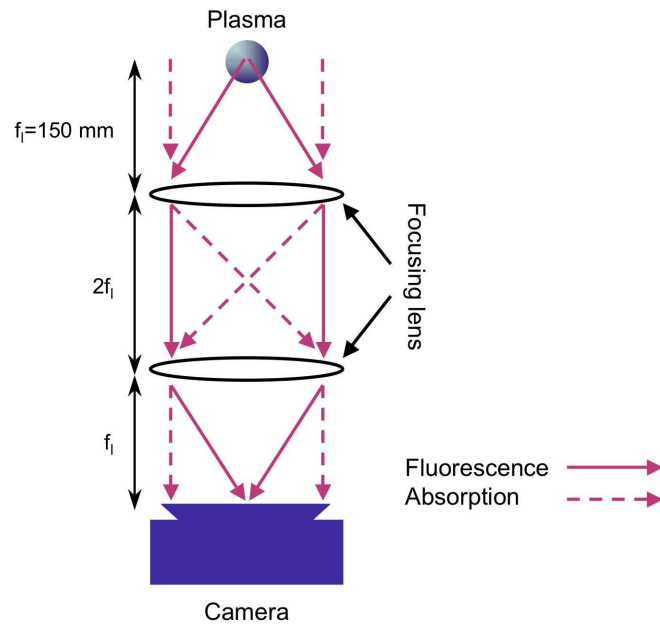


Figure C.1 : Optical layout showing ray tracing of both absorption and fluorescence beams.

element corresponds to three black lines separated by equally wide white lines. Table C.1 shows the number of line pairs per mm in the group and element.

As mentioned above, images of the shadow of the resolution target were taken with the absorption beam. Figure C.3 shows one of such images taken. The location of the resolution target was then changed in order to measure the resolution in different locations.

Images such as C.3 also allowed us to calibrate our pixel size. We conclude that one pixel corresponds to $13.14 \mu\text{m}$.

Continuing with the resolution of our imaging system, a measurement of resolution is shown in figure C.4. This figure shows a plot of the resolution measured along the x axis. To obtain this plot, the signal from the region of interest in the image

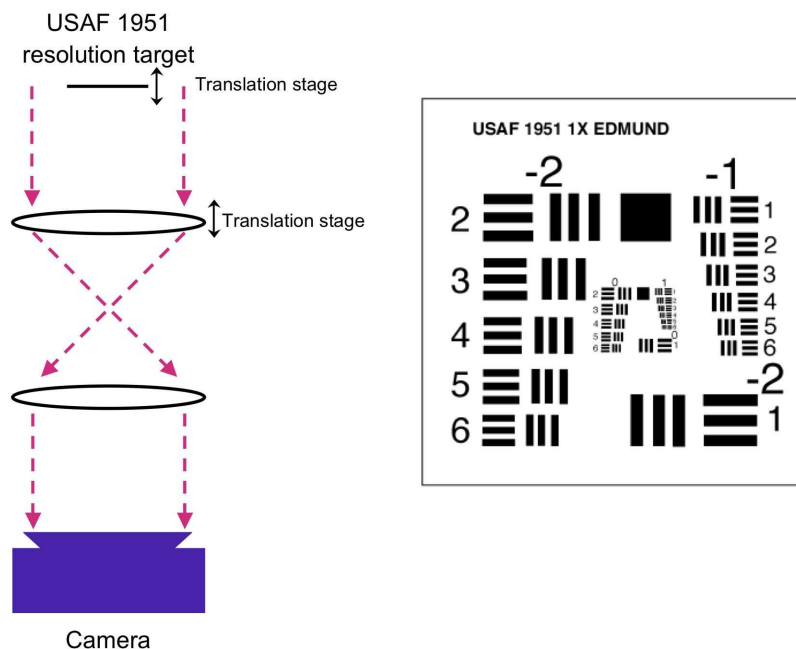


Figure C.2 : Placement of the USAF 1951 resolution target with respect to the imaging lenses. The target was placed in the center of the vacuum chamber in the position where the plasma would be located. It was set on a translation stage to be able to map out the resolution in different positions centered about this central location. One of the imaging lenses was also set on a translation stage to optimize the resolution. The absorption beam was used to perform the measurements. The figure also shows an image of the resolution target to the right. Resolution is measured by the ability to resolve line pairs within the target.

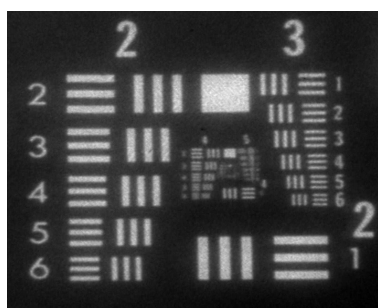


Figure C.3 : Example of images obtained. This image corresponds to the center elements of the resolution target seen in Fig. C.2.

Group →	-2	-1	0	1	2	3	4	5	6	7
Element ↓										
1	0.250	0.500	1.00	2.00	4.00	8.00	16.00	32.0	64.0	128.0
2	0.280	0.561	1.12	2.24	4.49	8.98	17.95	36.0	71.8	144.0
3	0.315	0.630	1.26	2.52	5.04	10.10	20.16	40.3	80.6	161.0
4	0.353	0.707	1.41	2.83	5.66	11.30	22.62	45.3	90.5	181.0
5	0.397	0.793	1.59	3.17	6.35	12.70	25.39	50.8	102.0	203.0
6	0.445	0.891	1.78	3.56	7.13	14.30	28.50	57.0	114.0	228.0

Table C.1 : Number of line pairs per mm in the USAF 1951 resolution target.

was integrated along the y direction. This plot specifically corresponds to Group 5, Elements 6 to 1 (from left to right on the plot). It can be clearly seen that our imaging system cannot resolve the lines that correspond to elements 4 – 6. The best resolution in this example is therefore Group 5, Element 3. Looking at table C.1, this corresponds to 40.3 line pairs per mm. The smallest object that could be resolved in this location would then be $1/(2 \times 40.3) = 12.4 \times 10^{-3}$ mm or $12.4 \mu\text{m}$, where the factor of 2 accounts for the fact that the table lists line pairs per mm.

Once the measurement of resolution was performed at a particular position of the resolution target, the target was moved to a different location and the procedure was repeated. Figure C.5 shows the result of the resolution on different locations of the resolution target. In this plot the z position refers to the target being moved along the principal axis of the imaging system. The plot also shows three data sets, where

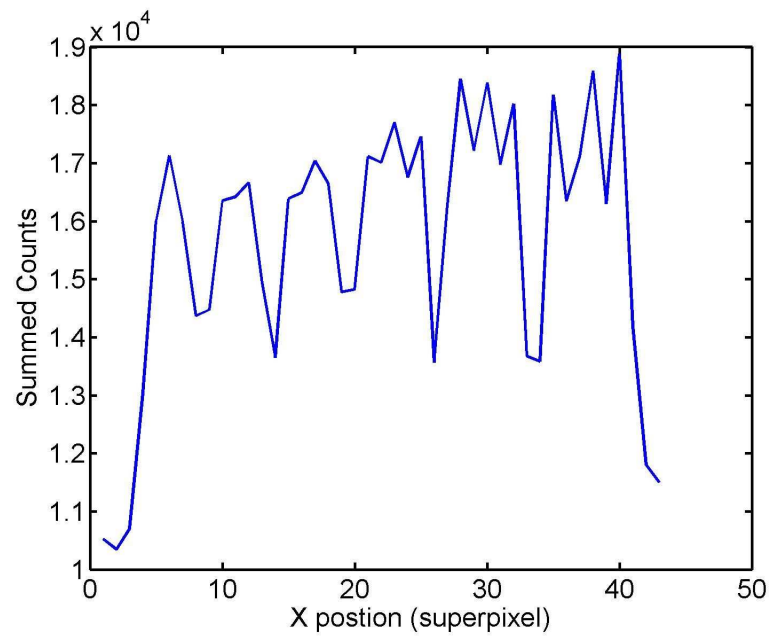


Figure C.4 : Example of a plot used to determine resolution. Summed counts corresponds to the integrated signal of the region of interest versus its position along the x direction. This plot corresponds to the signal originating from Elements 6 to 1 in Group 5 (from left to right on the plot). Clearly that last element we are able to resolve is Element 3. Looking at table C.1, this corresponds to 40.3 line pairs per mm or a resolution of $12.4 \mu\text{m}$.

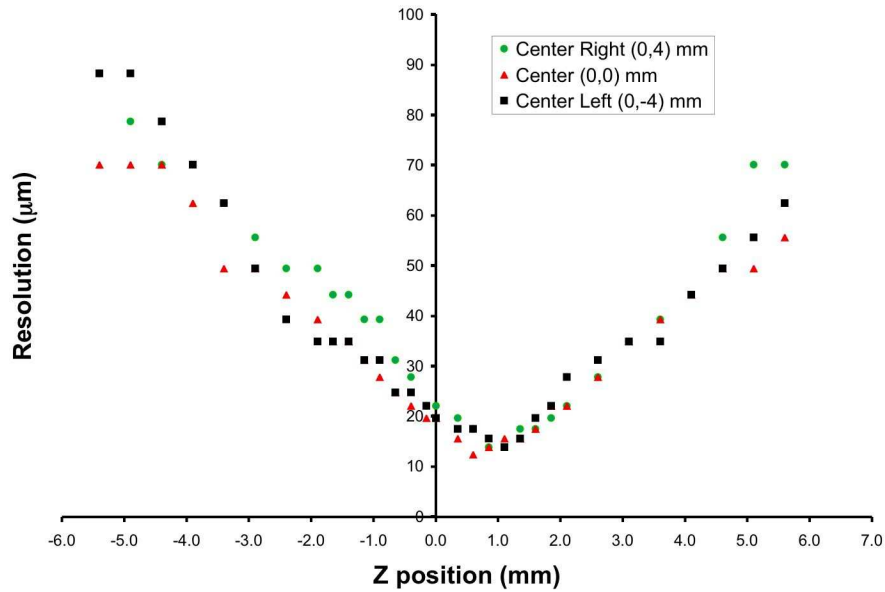


Figure C.5 : Measured resolution versus position of the resolution target. Here the z position refers to the target being moved along the principal axis of the imaging system. The plot only shows three data sets that correspond to three different locations along the $x - y$, however measurements were performed on a total of 12 locations with similar results.

each corresponds to a different location along the $x - y$ plane. For clarity, the plot only shows three data sets from three different locations along the $x - y$ plane, but measurements were performed on a total of 12 locations with very similar results.

From all the plots (similar to Fig. C.5) we concluded that the smallest feature that we could resolve would measure $12.4 \mu\text{m}$. Furthermore, figure C.5 shows that the maximum resolution does not change for different locations along the $x - y$ plane, as all three curves follow each other closely. The resolution does change along the z axis as expected (main axis of imaging system). This curve can thus help us gauge how much the resolution changes if the slit used for sheet fluorescence is not properly centered on the plasma. An improper centering of the slit by 1 mm would result in

a drastic drop in resolution by approximately a factor of 2. However, since the $1/e^2$ radius of the Gaussian plasma density profile is ~ 1 mm, an improper centering of the slit would result in noticeable drop in the expected signal (a drop to $\sim 13\%$) and could easily be noted and corrected.